Postprocessing subtraction of tilt-to-length noise in LISA

S. Paczkowski,[1,2,*] R. Giusteri,[1,2,†] M. Hewitson,[1,2] N. Karnesis,[3] E. D. Fitzsimons,[4] G. Wanner,[1,2] and G. Heinzel[1,2]

[1]*Max Planck Institute for Gravitational Physics (Albert Einstein Institute), D-30167 Hannover, Germany*
[2]*Leibniz Universität Hannover, D-30167 Hannover, Germany*
[3]*Department of Physics, Aristotle University of Thessaloniki, Thessaloniki 54124, Greece*
[4]*The UK Astronomy Technology Centre, Royal Observatory, Edinburgh, Blackford Hill, Edinburgh EH9 3HJ, United Kingdom*

(Received 5 April 2022; accepted 31 July 2022; published 15 August 2022)

The coupling of an angular jitter into the interferometric phase readout is summarized under the term tilt-to-length (TTL) coupling. This noise is expected to be a major noise source in the intersatellite interferometry for the Laser Interferometer Space Antenna (LISA) space mission. Despite efforts to reduce it by satellite construction, some remaining TTL noise will need to be removed in postprocessing on Earth. Therefore, such a procedure needs to be developed and validated to ensure the success of the LISA mission. This paper shows a method to calibrate and subtract TTL noise that has no impact on LISA science operations. This solution relies on noise minimization and uses the differential wavefront sensing (DWS) measurements to estimate the TTL contribution. Our technique is applied after the laser frequency noise is suppressed via the time-delay interferometry (TDI) postprocessing algorithm. We use a simulation to show as a proof-of-principle that we can estimate the TTL coefficients to the required accuracy level based on the current design configuration of LISA. We then use these estimates to subtract the TTL noise, ensuring that any remaining TTL noise is below the current estimate of the other noise sources. We validate the procedure on simulated data for different operating scenarios. Our work shows that it is indeed possible to estimate the effect of TTL coupling and subtract it *a posteriori* from the TDI data streams.

DOI: 10.1103/PhysRevD.106.042005

I. INTRODUCTION

LISA will be a space-based mission designed to detect gravitational waves over a frequency range from 0.1 mHz to 1 Hz. LISA is a space mission led by the European Space Agency and, at the time of writing, is transitioning to the mission phase B with an expected launch in the 2030s. It will consist of three spacecraft (SC) maintaining a nearly equilateral triangular formation and orbiting around the Sun, with arm-lengths of 2.5 million km [1]. Laser interferometers will measure the distance between free-falling test masses (TMs) hosted in each SC. These TMs will ideally be geodesic end mirrors for a single interferometric arm. The optical setup inside the SC is mainly composed of a telescope and an optical bench (OB). The OB hosts the components required for heterodyne readout of the relative distances. The combination of each telescope, OB, and corresponding TM form the moving optical sub-assembly (MOSA). This is illustrated in Fig. 1. In contrast to ground-based detectors, LISA's arms will have varying lengths. Consequently, the detector response will be highly affected by laser frequency noise. To solve this problem, an algorithm called TDI [2] is applied in postprocessing to synthesize virtual equal-armlength interferometers.

In addition to laser frequency noise, other effects can cause phase noise in the heterodyne interferometric readout. The TTL coupling, which is the coupling of an angular jitter into the interferometric phase readout, is one of these. This cross-coupling arises, for example, from misalignments within the optical system. It is not reduced by TDI. Unless mitigated otherwise, this noise source will affect the science performance of LISA.

TTL in LISA will be mitigated in several steps. Figure 2 shows the expected TDI output after each of these steps. It is expressed in terms of the square root of the power spectral density (PSD). As a first step, the overall misalignment will be reduced as much as possible in the design and construction phase. However, the required level of alignment of the optical components to completely mitigate TTL is technically impossible. The expected level of alignment

*sarah.paczkowski@aei.mpg.de
†roberta.giusteri@aei.mpg.de

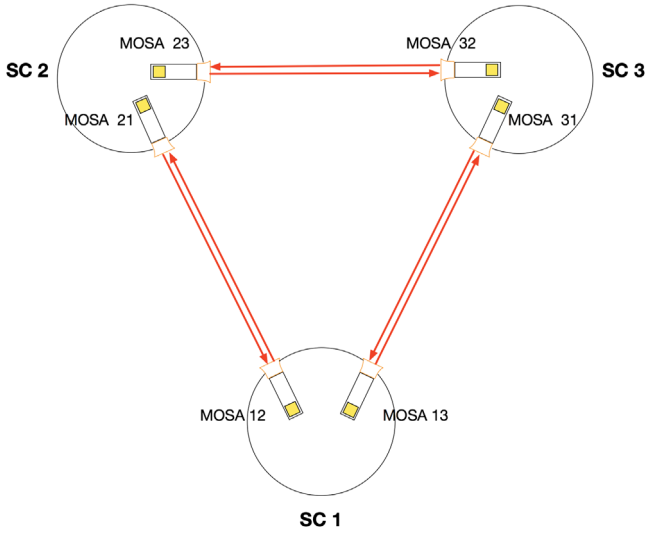

FIG. 1. Sketch of nomenclature and LISA intersatellite laser links. The test masses (TMs) are depicted by the yellow cubes inside the moving optical subassemblies (MOSAs). The telescopes are illustrated in orange. They are used to collect and send the laser beams, drawn here as red arrows. For clarity, we do not show the OBs and the interferometry on board the SC.

achieved after integration, is indicated by the pink line. Here we assume TTL at a level of 8.5 mm/rad for all contributors (compare Sec. II for a detailed description) and all other noise estimates according to the latest expectations (compare Sec. III for details). A set of optical parallel plates can be used to compensate for the alignment error. This set is called the beam alignment mechanism and it is foreseen to be integrated and adjusted on ground before launch. Figure 2 depicts a prediction of the effect of this alignment compensation in green. This prediction assumes now all TTL contributors at the level of 2.3 mm/rad and all other settings remain the same as in the scenario depicted in pink. In addition, misalignment can also arise during launch, transfer to orbit, and over time. The remaining TTL noise needs to be subtracted in postprocessing on ground via measurements of the angular jitters to fulfill the requirement indicated by the dashed gray line in Fig. 2.

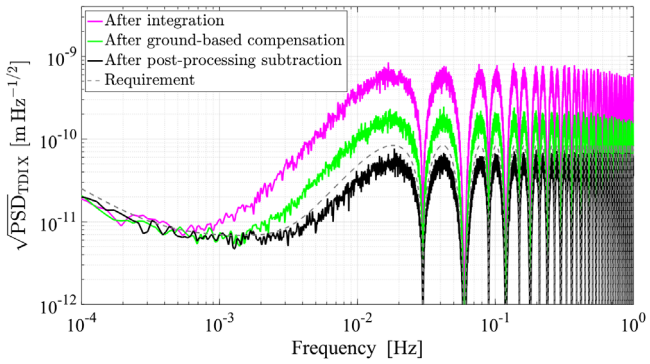

FIG. 2. The expected effect of TTL noise in the TDI X output for different stages of the LISA development and operations.

Indeed, this requirement is an overall constellation requirement. It results from combining the current requirement on the TM-to-TM displacement noise:

$$\sqrt{S_{\mathrm{disp}}^{\mathrm{req}}}(f) = 13.5\frac{\mathrm{pm}}{\sqrt{\mathrm{Hz}}}\sqrt{1+\left(\frac{2\ \mathrm{mHz}}{f}\right)^4}, \qquad (1)$$

with the current requirement on the residual acceleration noise on a single TM:

$$\sqrt{S_{\mathrm{acc}}^{\mathrm{req}}}(f) = 2.7\frac{\mathrm{fm}}{\mathrm{s}^2\sqrt{\mathrm{Hz}}}\sqrt{1+\left(\frac{0.4\,\mathrm{mHz}}{f}\right)^2}\sqrt{1+\left(\frac{f}{8\,\mathrm{mHz}}\right)^4}, \qquad (2)$$

via an analytic model of the TDI algorithm [3]. Equations (1) and (2) are expressed in terms of the square root of the PSD and f denotes the frequency dependency of the respective requirement. Therefore, considering the current alignment and jitter estimates, the target set by the LISA project is to estimate the individual TTL contributors, currently expected to be around 2.3 mm/rad, with an accuracy of ± 0.1 mm/rad. Assuming this accuracy level is reached, we obtain the black trace, and all other settings remain the same as in the two other scenarios. The black curve in Fig. 2 is dominated by acceleration noise at frequencies up to a few mHz and by other interferometric readout noises, at higher frequencies. The residual TTL noise is a small contribution, and its level will be discussed in Sec. IV A. The noise levels of Fig. 2 result from a LISA simulation which will be described in Sec. III.

This paper demonstrates a proof-of-principle that we can estimate the TTL coupling coefficients to the required accuracy level based on the current design configuration of LISA and subtract TTL noise to be below the current estimate of the other noise sources. In Sec. II, we provide a model for TTL of a LISA MOSA and the details of how we estimate the TTL contribution. We use a simulator to test and validate the estimation and subtraction of TTL noise. This simulator and its configuration are described in Sec. III. Next, Sec. IV, shows that we can estimate the TTL coupling coefficients to the required accuracy level and subtract TTL noise. This result is further validated for different operating scenarios in Sec. V. We summarise our results in Sec. VI. The limits and possible extensions of our approach are summarized in Sec. VII.

II. TTL NOISE SUBTRACTION IN LISA

Let us consider geometric TTL coupling associated to a TM as an example to start with. In this case, geometric TTL coupling originates from the coupling of an arbitrary TM tilt, α, into the optical path length. This effect is produced by an offset between TM rotation point and the laser beam reflection point, y. The change in path length, δp, can be approximated to first order as: $\delta p \approx y \cdot \alpha$ (for $\alpha \ll 1$) [4,5]. Figure 3(a)

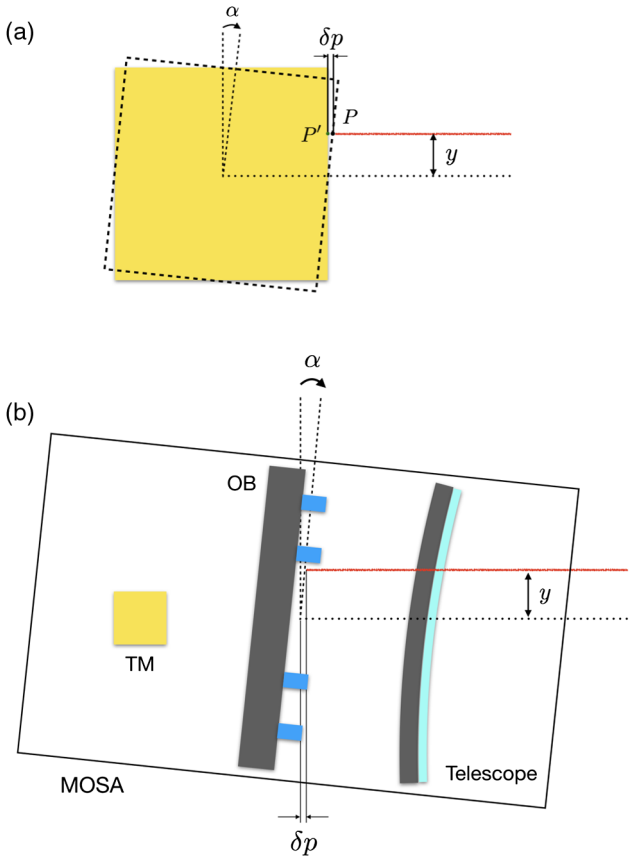

FIG. 3. (a) Example of geometric TTL coupling. In the presence of an offset y of the incident laser beam, the angular jitter of the TM, α, produces a change in the optical path length, δp. (b) An example of geometric TTL coupling in LISA. The angular jitter of the MOSA, α couples with an off-axis laser beam emitted (offset y) from the distant SC. The effect of this is a change in the optical path length, δp. In this simplified example the rotation point coincides with the MOSA center of mass.

depicts an example. Considering two angular degrees of freedom of the TM, η (corresponding to pitch) and φ (corresponding to yaw), the change in path length due to TTL coupling, δp, can be described by the following equation which is approximately linear in each degree of freedom:

$$\delta p = C_\eta \cdot \eta + C_\varphi \cdot \varphi, \tag{3}$$

where C_η and C_φ are the respective coupling coefficients. Within this paper, we consider accumulated TTL effects that are mixed of geometric and nongeometric contributions. We, therefore, extend this equation to include also nongeometric effects. Equation (3) then reads the very same, only that δp is not the optical pathlength change in the system, but instead the total phase change converted to a length.

A. MOSA TTL noise

Let us now move to the LISA case. In LISA, the changes in the distance between two TMs at the end of an arm result from the combination of three interferometric signals. On each MOSA, a TM interferometer detects the distance variations between the TM and its local OB. These two measurements are combined with the intersatellite interferometer (ISI) measurement of the changes in the distance between the two OBs, which are 2.5 million km apart. Each OB also incorporates a reference interferometer to compare the two local laser beams aboard the same SC.

TTL coupling is a major source of noise in the TDI output data streams, as visible from Fig. 2, and it is mainly driven by the MOSA angular jitter relative to the inertial reference, which is the incoming beam. Therefore, in this publication, we will focus on TTL in the ISI. TTL in the other interferometers is discussed in [6]. In the ISI, the coupling between an angular offset and a lateral jitter into the optical path length is not considered here because it is significantly smaller with respect to the TTL we consider. Figure 3(b) provides a simplified example of the TTL in the ISI. Thus, following Eq. (3), TTL noise in the ISI on one MOSA can be modeled by the equation below, which applies to a generic MOSA ij, with $i, j = 1, 2, 3$:

$$x_{\mathrm{TTL}_{ij}} = C_{ij\eta} \cdot \eta_{ij} + C_{ij\varphi} \cdot \varphi_{ij}, \tag{4}$$

where η_{ij} and φ_{ij} are the MOSA jitters relative to the inertial space along $k = \eta, \varphi$ degrees of freedom, respectively, and the coefficients C_{ijk} are the associated coupling factors. The MOSAs are mounted on a hinge to enable yaw rotation. Under normal operating conditions, the remaining pitch rotation is already small compared to the yaw but this way of mounting should prevent the MOSA from rolling with respect to the satellite. Therefore, along the roll angle θ the MOSAs are assumed to be infinitely stiff in this model. Thus, Eq. (4) models TTL noise as a linear combination of the MOSA jitters and nonlinear terms are assumed negligible. We can justify this because we can linearize TTL around different working points.

In addition, we split the TTL coupling, measured in each MOSA, into the effect associated with the incoming beam on the respective MOSA (Rx) and the outgoing beam from the far MOSA along the same arm (Tx), as represented by the index l. The optical path length noise generated in the distant MOSA needs to be delayed when measured in the local MOSA according to the light travel time along this link. This delay is denoted $\mathcal{D}_{ij}$. The index ij indicates here the MOSA where the respective arm ends. For the case of constant coupling coefficients, the delay is applied to the respective jitter. Thus, Eq. (4) becomes:

$$\begin{aligned} x_{\mathrm{TTL}_{ij}} = {} & C_{ij\eta\mathrm{Rx}} \cdot \eta_{ij} + C_{ji\eta\mathrm{Tx}} \cdot \mathcal{D}_{ij}\eta_{ji} \\ & + C_{ij\varphi\mathrm{Rx}} \cdot \varphi_{ij} + C_{ji\varphi\mathrm{Tx}} \cdot \mathcal{D}_{ij}\varphi_{ji}. \end{aligned} \tag{5}$$

So, we can now define the associated TTL coefficients C_{ijkl} with $i, j = 1, 2, 3$, $k = \eta, \varphi$ and $l = \mathrm{Rx}, \mathrm{Tx}$.

The model of the induced noise is based upon Eq. (5). However, the true MOSA jitters will not be known, but only the measured jitters will be available. Here, we model these as the true jitters with additive sensing noise. Indeed, the angular measurements in the ISI will be done via the differential wavefront sensing (DWS) technique [7]. Accordingly, the angles result from comparing the tilt of the wavefront of the local laser beam and the beam originating at the far satellite. The DWS measurement is calibrated to deliver angles in inertial space frame, that means the calibration accounts for the magnification of the telescope, for example. Therefore, we call the η_{ij} measurement when the sensing noise, n^{DWS}, is included as follows:

$$\eta_{ij}^{\mathrm{DWS}} = \eta_{ij} + n^{\mathrm{DWS}}. \tag{6}$$

And similarly for $\varphi_{ij}^{\mathrm{DWS}}$. Consequently, Eq. (5) reads:

$$\begin{aligned}\hat{x}_{\mathrm{TTL}_{ij}} = {} & C_{ij\eta\mathrm{Rx}} \cdot \eta_{ij}^{\mathrm{DWS}} + C_{ji\eta\mathrm{Tx}} \cdot \mathcal{D}_{ij}\eta_{ji}^{\mathrm{DWS}} \\ & + C_{ij\varphi\mathrm{Rx}} \cdot \varphi_{ij}^{\mathrm{DWS}} + C_{ji\varphi\mathrm{Tx}} \cdot \mathcal{D}_{ij}\varphi_{ji}^{\mathrm{DWS}},\end{aligned} \tag{7}$$

where, compared to the model of Eq. (5), the $\hat{}$ symbol indicates TTL noise as estimated from the measured jitters. In Fig. 1 we can see that LISA has 6 such MOSAs, two on each satellite. From Eq. (7) we see that we have 4 TTL coefficients to consider for each of these which results in a total of 24 TTL coefficients.

As mentioned in the previous section, laser frequency noise will dominate the relative distance measurements of the LISA ISI by several orders of magnitude. Thus, estimation of the TTL coupling coefficients is only possible after suppressing the laser frequency noise. The postprocessing algorithm which achieves this in LISA is called TDI [2,8]. A key feature of the TDI algorithm is that it time-shifts and combines the interferometric measurements on board different satellites of the LISA constellation. We will summarize some key information about TDI here which is essential for understanding the approach. Let us consider a generic signal $\Psi(t)$ that needs to be time-shifted, or in other words delayed, by the light travel time along the respective arm, L_{ij}, at a certain moment in time. We then write [2]:

$$\mathcal{D}_{ij}\Psi(t) = \Psi(t - L_{ij}(t)). \tag{8}$$

When a measurement has to be delayed two times, it results in:

$$\begin{aligned}\mathcal{D}_{pq}\mathcal{D}_{ij}\Psi(t) &= \Psi(t - L_{pq}(t) - L_{ij}(t - L_{pq}(t))) \\ &\simeq \Psi(t - L_{pq}(t) - L_{ij}(t) + \dot{L}_{ij}(t)L_{pq}(t)).\end{aligned} \tag{9}$$

To cancel laser frequency noise to first order of SC separation velocity, $\dot{L}_{ij}$, the so-called 2nd generation Michelson TDI combinations (TDI 2.0) are applied to the data [2]. Here we report the expression for the TDI 2.0 output X which reflects the two round trips illustrated and combined as in Fig. 4:

$$\begin{aligned}X &= \mathrm{TDI}X(\bar{\eta}_{13}, \bar{\eta}_{31}, \bar{\eta}_{12}, \bar{\eta}_{21}) \\ &= (1 - \mathcal{D}_{12}\mathcal{D}_{21} - \mathcal{D}_{12}\mathcal{D}_{21}\mathcal{D}_{13}\mathcal{D}_{31} \\ &\quad + \mathcal{D}_{13}\mathcal{D}_{31}\mathcal{D}_{12}\mathcal{D}_{21}\mathcal{D}_{12}\mathcal{D}_{21}) \cdot (\bar{\eta}_{13} + \mathcal{D}_{13}\bar{\eta}_{31}) \\ &\quad - (1 - \mathcal{D}_{13}\mathcal{D}_{31} - \mathcal{D}_{13}\mathcal{D}_{31}\mathcal{D}_{12}\mathcal{D}_{21} \\ &\quad + \mathcal{D}_{12}\mathcal{D}_{21}\mathcal{D}_{13}\mathcal{D}_{31}\mathcal{D}_{13}\mathcal{D}_{31}) \cdot (\bar{\eta}_{12} + \mathcal{D}_{12}\bar{\eta}_{21})\end{aligned} \tag{10}$$

where the input measurements, $\bar{\eta}_{ij}$, are intermediate variables in the TDI algorithm [8]. Then, the remaining laser frequency

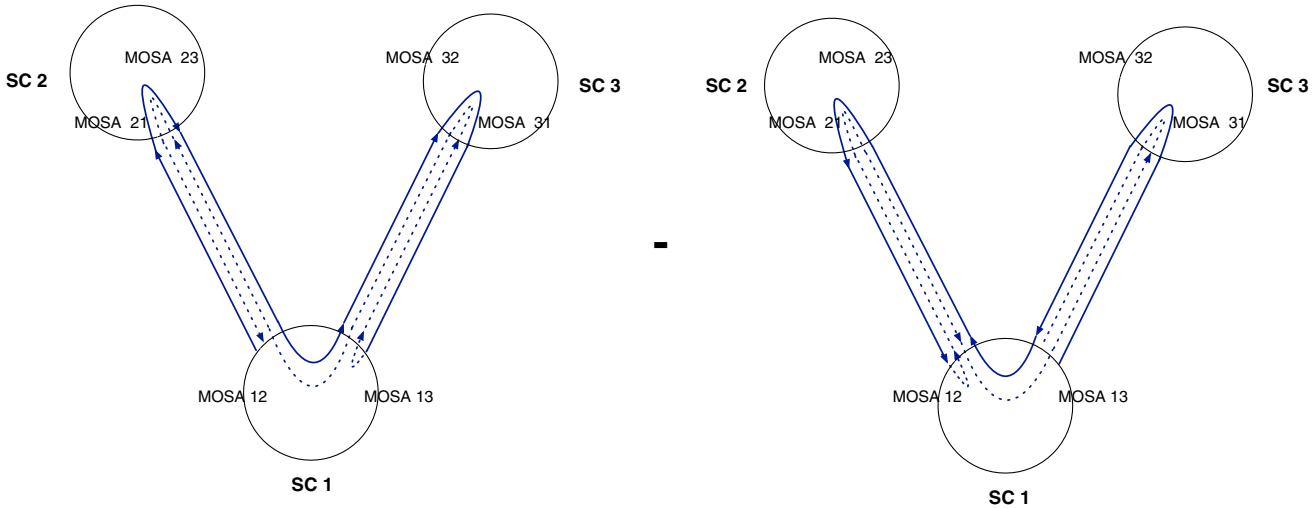

FIG. 4. Visualization of the two synthetic optical paths which are constructed and combined, via the "-" sign, in TDI 2.0 postprocessing to form the X combination [9].

noise is suppressed via TDI as in Eq. (10) and the gravitational wave signal can be extracted. In addition to X, we consider two more TDI combinations, Y and Z, centered around SC 2 and SC 3, respectively. Their expressions can be obtained from Eq. (10) by cyclic permutation of the indices.

As stated above, besides the other noises of the system, we need to propagate through TDI the TTL noise generated by our model in Eq. (7). This will be described in detail in Sec. II B. A more detailed description, including an analytical model for TTL noise coupling in TDI X, is given in [6,10]. In essence, the TDI algorithm will propagate and combine the 24 coupling coefficients. In other words, it will not be possible to estimate just a single coefficient, but we always have to deal with the combined impact of several coupling factors. In addition, as visible from Fig. 4, in TDI X all coupling coefficients related to MOSA 23 and MOSA 32 have no impact. Indeed, only the TTL noise caused by the jitter of MOSA 21, 12, 13, and 31 in η and φ will appear in this combination. This is illustrated in Fig. 4. Therefore, we can only access 16 of the 24 TTL coupling coefficients with X alone. The same also applies to the Y and Z combinations. Accordingly, to estimate all 24 coefficients, we combine X, Y, and Z.

The details of the coefficient estimation procedure will be discussed in the next paragraph.

B. TTL coefficient estimation and noise subtraction

Even though we cannot estimate the TTL coupling coefficients individually, the linearity of the TTL model and TDI expressions allows us to model the contribution of TTL noise to the TDI outputs as the sum of 24 contributions. This is the key idea of the TTL model we use for subtraction in this work. Indeed, on the timescale considered for the TTL coefficient estimation (24 hours, see Sec. III), the changes in the SC separation are at a level of 0.035%,[1] and thus, they are assumed negligible. In other words, $\dot{L}_{ij}(t) \simeq 0$ and Eq. (9) becomes:

$$\mathcal{D}_{pq}\mathcal{D}_{ij}\Psi(t) \simeq \Psi(t - L_{pq} - L_{ij}). \tag{11}$$

As a consequence, multiple delays are linear functions of L_{ij} and the TDI expressions are linear in L_{ij} as well [see Eq. (10)]. Under this assumption, the delay operators commute. This linear approach is computationally more efficient than using the full expression and fits naturally to the timescale under consideration in this proof-of-principle activity.

After we have seen that we can indeed linearize TDI for our purpose, let us now describe the linear TTL in TDI model. Again, this model uses the 24 contributors and we proceed as follows: We calculate each of the TTL contributions by replacing a single coefficient with a scale factor β while the remaining 23 coefficients are equal to 0. For example, for the case of $i = 1$, $j = 2$, $k = \eta$ and $l = \mathrm{Rx}$, we consider the coefficient $C_{12\eta\mathrm{Rx}}$, and then Eq. (7) would read:

$$\begin{aligned}\hat{x}_{\mathrm{TTL}_{C_{12\eta\mathrm{Rx}}}} &= \beta \cdot \eta_{12}^{\mathrm{DWS}} + 0 \cdot \mathcal{D}_{12}\eta_{21}^{\mathrm{DWS}} \\ &\quad + 0 \cdot \varphi_{12}^{\mathrm{DWS}} + 0 \cdot \mathcal{D}_{12}\varphi_{21}^{\mathrm{DWS}}.\end{aligned} \tag{12}$$

Then Eq. (12) is propagated through TDI as in Eq. (10) to yield the three TTL contributions in TDI for the coefficient $C_{12\eta\mathrm{Rx}}$. For this example coefficient, we thus have for X, Y and Z:

$$\begin{aligned}\mathrm{TDI}X(\hat{x}_{\mathrm{TTL}_{C_{12\eta\mathrm{Rx}}}}) &= X^{\mathrm{TTL}}_{C_{12\eta\mathrm{Rx}}} = -((\mathcal{D}_{13}\mathcal{D}_{31} - 1) \cdot (\mathcal{D}_{12}\mathcal{D}_{13}\mathcal{D}_{21}\mathcal{D}_{31} - 1)) \cdot \eta_{12}^{\mathrm{DWS}} \cdot C_{12\eta\mathrm{Rx}}, \\ \mathrm{TDI}Y(\hat{x}_{\mathrm{TTL}_{C_{12\eta\mathrm{Rx}}}}) &= Y^{\mathrm{TTL}}_{C_{12\eta\mathrm{Rx}}} = (\mathcal{D}_{21}(\mathcal{D}_{23}\mathcal{D}_{32} - 1) \cdot (\mathcal{D}_{12}\mathcal{D}_{21}\mathcal{D}_{23}\mathcal{D}_{32} - 1)) \cdot \eta_{12}^{\mathrm{DWS}} \cdot C_{12\eta\mathrm{Rx}}, \\ \mathrm{TDI}Z(\hat{x}_{\mathrm{TTL}_{C_{12\eta\mathrm{Rx}}}}) &= Z^{\mathrm{TTL}}_{C_{12\eta\mathrm{Rx}}} = 0.\end{aligned} \tag{13}$$

The same procedure is repeated for all 24 coefficients. Thus, we can write:

$$\begin{aligned}\mathrm{TDI}X(\hat{x}_{\mathrm{TTL}_{C_{ijkl}}}) &= X^{\mathrm{TTL}}_{C_{ijkl}}, \\ \mathrm{TDI}Y(\hat{x}_{\mathrm{TTL}_{C_{ijkl}}}) &= Y^{\mathrm{TTL}}_{C_{ijkl}}, \\ \mathrm{TDI}Z(\hat{x}_{\mathrm{TTL}_{C_{ijkl}}}) &= Z^{\mathrm{TTL}}_{C_{ijkl}},\end{aligned} \tag{14}$$

with $i, j = 1, 2, 3$, $\mathrm{k} = \eta, \varphi$ and $l = \mathrm{Rx}, \mathrm{Tx}$. Note that the contributions in Eq. (13) and Eq. (14) contain the scale factor β and not the corresponding coefficient value. Accordingly, there is a total of $3 \times 24 = 72$ precomputed TTL in TDI terms. Since only four of the six MOSAs contribute to each of the three Michelson TDI outputs X, Y, Z, only 16 of the 24 TTL coefficient contributions are different from 0 in each X, Y, and Z. Since two links are common to each pair of two TDI combinations, a different set of 8 coefficients is shared between X and Y, Y and Z, X and Z, respectively. Consequently, each coefficient appears in two TDI combinations. In this proof-of-principle activity, we focus on the nominal operation mode with all arms active. To minimize the correlation between X, Y,

[1]We obtain a maximum change in arm length of around 875 km in a day, considering five years of flight and trailing orbits. The calculation is based upon [11].

and Z, an alternative set of TDI combinations can be used for the coefficient estimation. These are the so-called A, E, and T channels which are linear combinations of X, Y, and Z [12] as follows:

$$A = \frac{1}{\sqrt{2}}(Z - X),$$
$$E = \frac{1}{\sqrt{6}}(X - 2 \cdot Y + Z),$$
$$T = \frac{1}{\sqrt{3}}(X + Y + Z). \tag{15}$$

Therefore, to estimate the coefficients, we combine all the measurement data available, which corresponds here to TDI A, E, and T and use all precomputed TTL in TDI terms as of Eq. (14). The minimization is performed using the discrete Fourier transform of the data and the cost function reads:

$$\sum_f \left(\mathrm{abs}\left(\tilde{A} - \sum_{m=1}^{24} C_{ijkl} \tilde{A}^{\mathrm{TTL}}_{C_{ijkl}} \right)^2 + \mathrm{abs}\left(\tilde{E} - \sum_{m=1}^{24} C_{ijkl} \tilde{E}^{\mathrm{TTL}}_{C_{ijkl}} \right)^2 + \mathrm{abs}\left(\tilde{T} - \sum_{m=1}^{24} C_{ijkl} \tilde{T}^{\mathrm{TTL}}_{C_{ijkl}} \right)^2 \right), \tag{16}$$

where sum over f is a sum over frequencies and $\tilde{}$ indicates the discrete Fourier transform. The index m is counting all possible combinations of i, j, k, l from $m = 1 = 12\eta\mathrm{Rx}$ until $m = 24 = 32\varphi\mathrm{Tx}$. The frequency range used is from 1×10^{-3} Hz to 0.1175 Hz with the exception of the frequency bins around the nulls at 0.03, 0.06, and 0.09 Hz (see Fig. 7). In addition, we use a current estimate of the expected remaining noise after the application of TDI without the TTL noise contribution to whiten the data. Details on this estimate are given in Appendix A. This estimate is fixed in the method presented here and is not part of the minimization. This simple whitening procedure justifies the choice of the frequency domain over the time domain. An MCMC (Markov Chain Monte-Carlo) algorithm [13,14] is applied, which also allows us to estimate the covariance between the resulting TTL coefficients.

In summary, to mitigate the remaining TTL noise in postprocessing, we start with a linear model of the expected contribution. We then estimate the 24 coupling coefficients and subtract the time series, which result from combining the coefficients with the precomputed terms, from the TDI time series. Let us point out more explicitly that both time series are subject to the same delays because both have been propagated through Eq. (10). In the following sections, we want to test and validate this procedure on simulated data. In the case of simulated data, the true coefficients, C_{ijkl}, are known. This allows us to compare the estimated values with the true values and compare to the required accuracy of 0.1 mm/rad. Let us define the deviation, δC_{ijkl}, as the difference between the estimated ($\hat{C}_{ijkl}$) and true coefficients (C_{ijkl}):

$$\delta C_{ijkl} = \hat{C}_{ijkl} - C_{ijkl}. \tag{17}$$

For instance, the expression of TDI X corrected using the coefficients estimated from the MCMC reads:

$$X^{\mathrm{MCMC}}_{\mathrm{corr}} = X - \sum_{m=1}^{24} \hat{C}_{ijkl} X^{\mathrm{TTL}}_{C_{ijkl}} = X - \sum_{m=1}^{24} (C_{ijkl} + \delta C_{ijkl}) X^{\mathrm{TTL}}_{C_{ijkl}}. \tag{18}$$

Section IV shows the results on simulated LISA data.

III. SIMULATION SETUP

We use a simulator called LISASim, which estimates optical phases to simulate the LISA constellation. The simulator uses beam equations expressed in displacement to compute the various interferometer outputs. It is an open-loop simulator and thus has the structural form of input noise mapped to measurements. LISASim includes the essential noise sources for this analysis, and their levels rely on the current LISA noise budget (see Appendix B). The simulator also implements TTL coupling in the TM interferometer and ISI. TTL noise in the TM interferometer is set to 0 for all datasets studied in this paper. For the ISI, TTL noise is simulated with all 24 coefficients having the same constant value of 2.3 mm/rad. This choice approaches a worst-case scenario with all coefficients having the same common amplitude. This TTL coupling coefficient is a sum of several effects. It considers, e.g., the currently budgeted misalignments of the telescope and the optical bench. Additionally, it includes, for example, also wavefront error coupling in the Tx coefficients as described by [15,16], plus a margin for each coefficient. The value of 2.3 mm/rad is estimated after the beam alignment mechanism was used to reduce the total effect (as depicted in green in Fig. 2). As described in Sec. II A, the MOSA angular measurements are generated with the additive sensing noise and TTL noise is computed as in Eq. (7). The simulator further assumes a fixed, nonrotating constellation but takes different arm lengths into account. Furthermore, we also assume perfectly timestamped data across the constellation, which means we have perfect and synchronized clocks. The TDI data streams are calculated from the simulated data in a second step. This means, we mimic the downlink in such a way that the TDI computation uses only the available telemetry. However, the simulation neglects the estimation of the arm lengths from the telemetry data. For more details see [17]. Instead, we

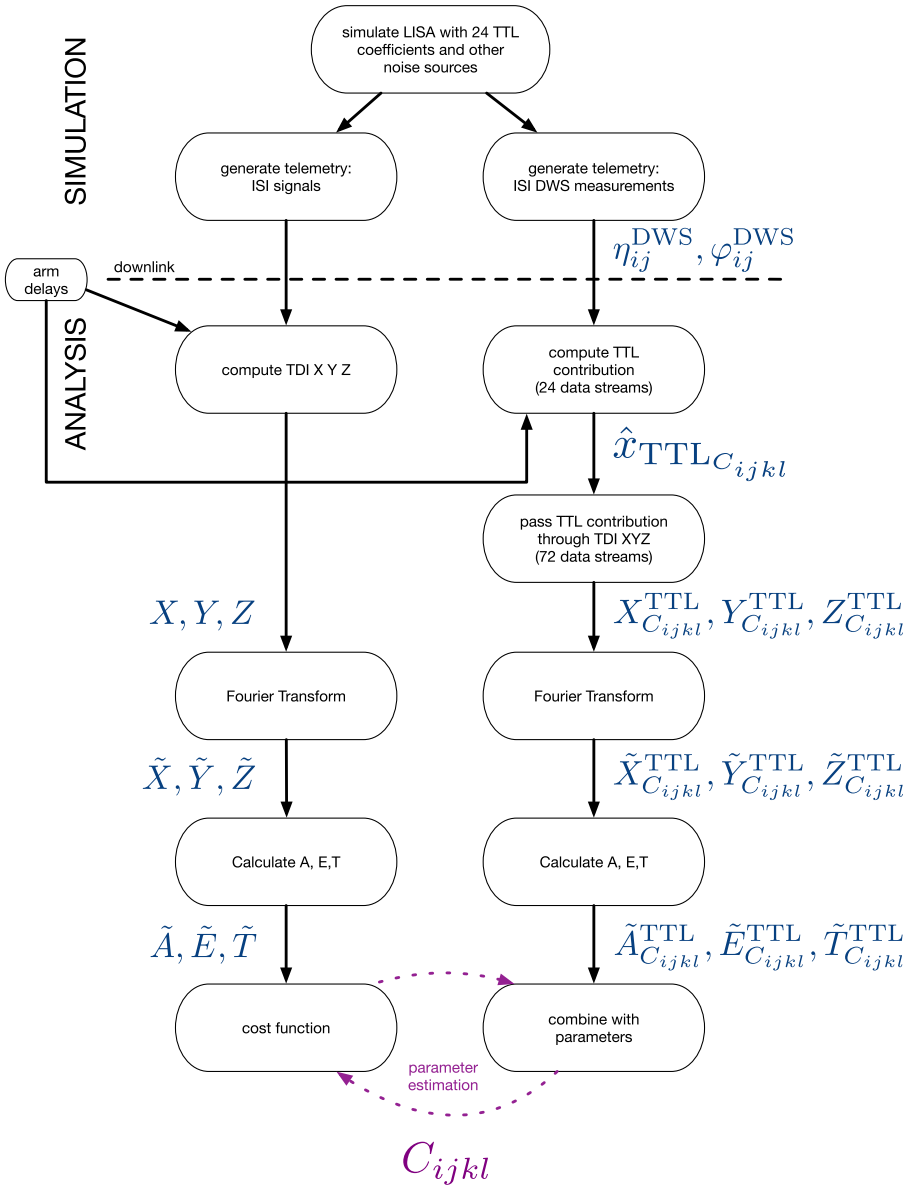

FIG. 5. Schematic of the simulation and data analysis steps. Refer to the text for an explanation of the symbols.

assume perfect knowledge of the arm lengths. The simulation, as well as the subsequent data analysis, use the MATLAB$^{\mathrm{TM}}$ toolbox LTPDA [18].

A detailed schematic of both the simulation and data analysis process is reported in Fig. 5 to put the previously explained procedure into context. As visible in the upper section, the TTL coupling coefficients and various noise sources can be simulated. Then, the interferometer measurements for each MOSA, also containing the noise terms as configured, are generated as part of the telemetry. In the same diagram, we show the angular measurements of the ISI separately in the second column on the right because these measurements are key to the TTL removal. The subtraction procedure described in Sec. II B is shown below the dashed line in Fig. 5. As visible on the left side, TDI X, Y, and Z are computed using the arm delays. In parallel, 24 TTL contributions are computed as linear combinations of measured and delayed DWS data, as in Eq. (7). Then, we apply the TDI algorithm to the TTL contributions only to get 72 data streams as in Eq. (14). Next, we apply Eq. (15) to then obtain the 24 TTL coefficients, C_{ijkl}, by minimizing the difference as in Eq. (16).

We perform the TTL coefficient estimation on one-day-long simulated datasets. Indeed, we expect that within a timescale of 24 hours, fixed coupling coefficients are sufficient to minimize TTL noise below the current estimate of the other noise sources. The simulator is set to generate data at 12 or 16 Hz, which are then downsampled to 0.5 Hz to produce telemetry data. LISA will implement a phase-locking scheme to keep the beat notes

of the ISI in the measurement band of the photoreceivers over the mission [19]. In practice, the primary laser is locked to a frequency reference, and all others are transponder-locked to the primary. Each laser may serve as the primary laser. Different schemes to lock the other five lasers to a primary laser are possible in LISA. The simulator implements these approximately. The locking is performed via the interferometer outputs. Thus, the locking will link the signal content between the interferometers. This is illustrated in Appendix C. Note that in this simulator, this applies only to the longitudinal measurements. However, the nominal configuration of the simulator considers six independent lasers which are assumed to be stabilized to the level reported in the Appendix B. Despite that no impact of the locking configuration on the TDI output could be found, a dedicated test of the coefficient estimation with different locking schemes will be presented in Sec. V B.

IV. RESULTS

As reported in Sec. III, the simulated data reflects the configuration based on the current design of the mission. The results presented here thus consider the 24 TTL coefficients having the same constant value (2.3 mm/rad) and assume no phase-locking scheme is implemented. The MCMC results for the coefficient values and the associated errors, meaning the standard deviation, are presented in Table I. The percentage error, computed as the ratio between the error and the estimated value converted to a percentage, is included in the table. The table also displays the deviation to the true value as the difference between estimated and true value. As visible, the estimate of all coefficients is within the allocated 0.1 mm/rad accuracy. Let us define the RMS (root mean square) value of the deviation to the true values, δC_{ijkl} [see Eq. (17)], over the 24 coefficients, as:

$$\mathrm{RMS} = \frac{1}{\sqrt{24}} \sqrt{\sum_{m=1}^{24} \delta C_{ijkl}^2}. \tag{19}$$

For the results of this section, we obtain an RMS value of (0.035 ± 0.007) mm/rad.

It is important to remark that the results shown here correspond to a single noise realization. Therefore, we repeated this test with different noise realizations. Within 1σ, we find the deviation to be at or below 0.1 mm/rad for more than 98% of the coefficient results. The values in Table I are therefore representative. Other possible influences will be discussed in more detail in Sec. V. These results and the test cases discussed are very similar to the case of using X, Y, and Z in the minimization.

The variances and covariances of the results of Table I are shown in Fig. 6. We note three kinds of interdependencies between the coefficients: two coefficients on the same SC are anticorrelated and this is more prominent along φ, see for example $C_{12\varphi\mathrm{Tx}}$ and $C_{13\varphi\mathrm{Rx}}$. Another anticorrelation is between the respective _Rx and _Tx component, as in the case of $C_{12\varphi\mathrm{Tx}}$ and $C_{12\varphi\mathrm{Rx}}$. The third kind is a correlation between two _Rx or _Tx components on the same SC, as $C_{13\varphi\mathrm{Tx}}$ and $C_{12\varphi\mathrm{Tx}}$ for instance. To summarize, the interdependency of coefficients is driven by the relative levels of SC and MOSA jitter and the fact that two MOSAs share the same SC. More detailed investigations will follow. Since the current results are reported with standard deviations, they do not take into account the different kinds of correlation between the coefficients.

TABLE I. Coefficient values estimated by the MCMC method. The expected value for all the 24 coefficients is 2.3 mm/rad.

Coefficient	Value [mm/rad]	Error [mm/rad]	% Error [ ]	Deviation [mm/rad]
$C_{12\eta\mathrm{Rx}}$	2.2456	0.0237	1.057	-0.0544 ± 0.0237
$C_{13\eta\mathrm{Rx}}$	2.2988	0.0250	1.089	-0.0012 ± 0.0250
$C_{23\eta\mathrm{Rx}}$	2.3166	0.0254	1.097	0.0166 ± 0.0254
$C_{21\eta\mathrm{Rx}}$	2.3397	0.0251	1.072	0.0397 ± 0.0251
$C_{31\eta\mathrm{Rx}}$	2.2676	0.0249	1.097	-0.0324 ± 0.0249
$C_{32\eta\mathrm{Rx}}$	2.3267	0.0244	1.048	0.0268 ± 0.0244
$C_{12\varphi\mathrm{Rx}}$	2.3219	0.0386	1.661	0.0219 ± 0.0386
$C_{13\varphi\mathrm{Rx}}$	2.3017	0.0374	1.625	0.0017 ± 0.0374
$C_{23\varphi\mathrm{Rx}}$	2.2457	0.0371	1.65	-0.0542 ± 0.0371
$C_{21\varphi\mathrm{Rx}}$	2.2349	0.0340	1.52	-0.0651 ± 0.0340
$C_{31\varphi\mathrm{Rx}}$	2.2530	0.0367	1.631	-0.047 ± 0.037
$C_{32\varphi\mathrm{Rx}}$	2.2711	0.0373	1.644	-0.0289 ± 0.0373
$C_{12\eta\mathrm{Tx}}$	2.3037	0.0257	1.115	0.0037 ± 0.0257
$C_{13\eta\mathrm{Tx}}$	2.2861	0.0241	1.054	-0.0139 ± 0.0241
$C_{23\eta\mathrm{Tx}}$	2.2752	0.0267	1.174	-0.0248 ± 0.0267
$C_{21\eta\mathrm{Tx}}$	2.2572	0.0260	1.153	-0.0428 ± 0.0260
$C_{31\eta\mathrm{Tx}}$	2.3020	0.0248	1.08	0.002 ± 0.025
$C_{32\eta\mathrm{Tx}}$	2.2831	0.0254	1.113	-0.0169 ± 0.0254
$C_{12\varphi\mathrm{Tx}}$	2.2636	0.0379	1.676	-0.0364 ± 0.0379
$C_{13\varphi\mathrm{Tx}}$	2.2333	0.0373	1.67	-0.0666 ± 0.0373
$C_{23\varphi\mathrm{Tx}}$	2.3140	0.0362	1.565	0.014 ± 0.036
$C_{21\varphi\mathrm{Tx}}$	2.3430	0.0346	1.476	0.043 ± 0.035
$C_{31\varphi\mathrm{Tx}}$	2.2923	0.0375	1.636	-0.0077 ± 0.0375
$C_{32\varphi\mathrm{Tx}}$	2.3350	0.0376	1.612	0.035 ± 0.038

While the coefficient estimation shown in Table I represents an important result, it is crucial to prove that we can reduce the TTL noise in TDI. The evidence of this is presented in Fig. 7. The results for TDI Y and TDI Z are very similar to TDI X and are not reported here for clarity. In Fig. 7 the uncorrected TDI X data is indicated by the black line. Let us point out that because this measurement combines interferometric measurements, with sensing noises as given in Appendix B, TDI X is subject to longitudinal sensing noise but it is free of DWS sensing noise. The TTL noise contribution after TDI given by the true values (2.3 mm/rad) is shown in red. To obtain this data, we first calculate the TTL contribution from all

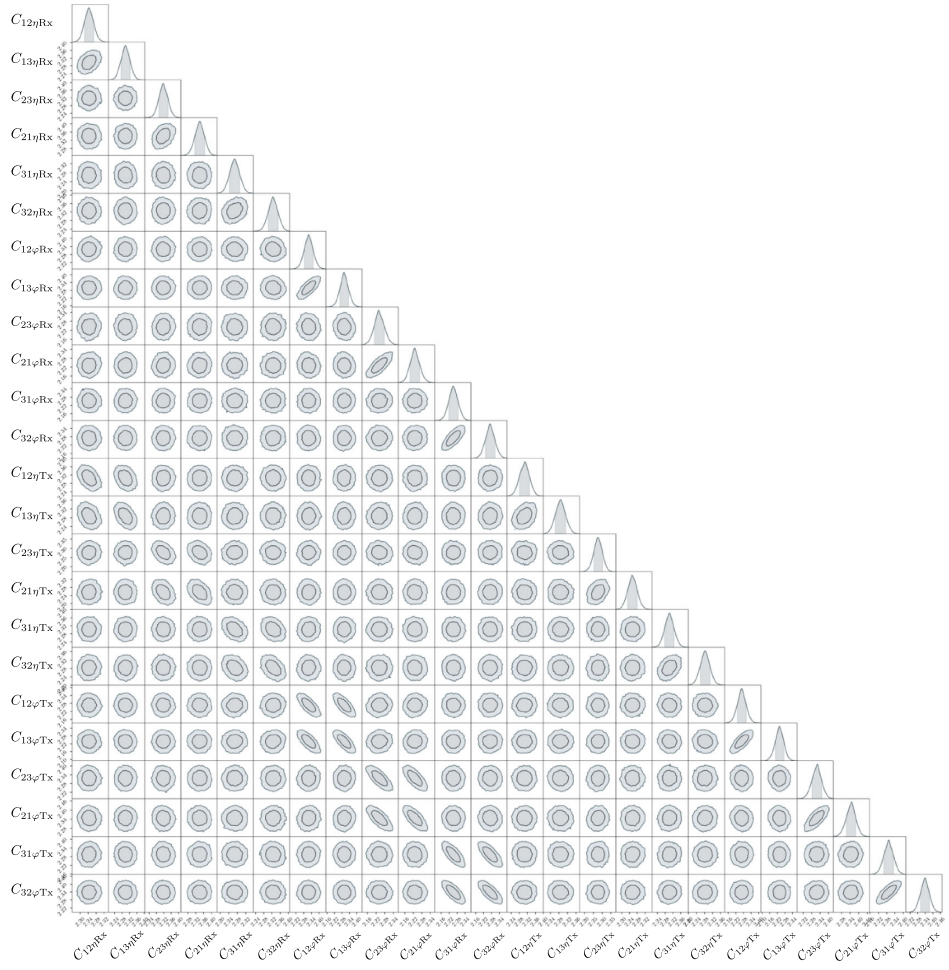

FIG. 6. Estimated variances and covariances of the results shown in Table I. This plot was produced using the CHAIN CONSUMER PYTHON package [20].

MOSAs as the sum of Eq. (7), evaluated for each of the six MOSAs. Then, we apply TDI as given in Eq. (10). The cyan curve is physically the result of subtracting the red curve from the black curve in time domain and then taking the square root of the PSD. However, here it is computed in a different way: First, we calculate the TTL contribution in TDI using the true coefficients values and the precomputed TTL in TDI terms [Eq. (14)]. Next, we take the difference of TDI X and the time series from the last step, similarly to Eq. (18). The cyan curve is then the square root of the PSD of this difference. Similarly, with the blue crosses, the subtraction of TTL using the MCMC results collected in Table I is shown. In this plot, the blue crosses are simply markers and do not reflect the uncertainties from Table I. To conclude, the TTL coefficients are estimated to the required accuracy and reduce TTL noise to the level achieved when the true values are used for the subtraction. More specifically, the difference between TDI corrected with true and estimated coefficient values, which is depicted in green in Fig. 7, is significantly below the remaining noise in TDI. To calculate this difference, we define:

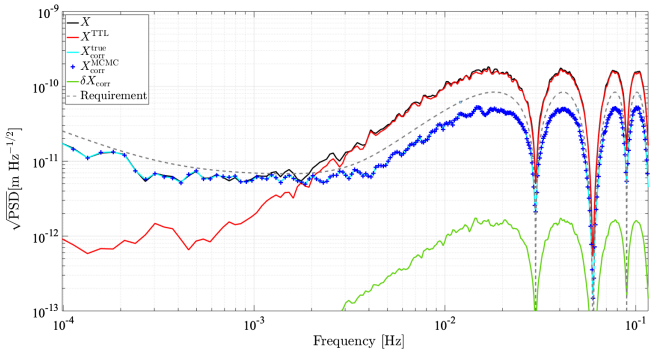

FIG. 7. TTL subtraction from TDI X (black) in terms of the square root of the PSD. The noise after subtraction using the estimated values (blue crosses) is comparable to the subtraction result assuming perfect knowledge of the simulated values (cyan). The difference between TDI X corrected with true and estimated coefficient values, δX_{corr}, is depicted in green.

$$X^{\mathrm{true}}_{\mathrm{corr}} = X - \sum_{m=1}^{24} C_{ijkl} X^{\mathrm{TTL}}_{C_{ijkl}}, \tag{20}$$

which denotes TDI X corrected using the true coefficient values. Therefore, the difference, $\delta X_{\rm corr}$, results from subtracting Eq. (18) from Eq. (20):

$$\delta X_{\rm corr} = X^{\rm true}_{\rm corr} - X^{\rm MCMC}_{\rm corr} = \sum_{m=1}^{24} \delta C_{ijkl} X^{\rm TTL}_{C_{ijkl}}, \quad (21)$$

with again $X^{\rm TTL}_{C_{ijkl}}$ as the precomputed TTL in TDI contribution. Applying TDI to the TTL contributors as from Eqs. (6) and (7), we can define:

$$\mathrm{TDI}X(n^{\rm DWS}) = X^{n^{\rm DWS}}, \qquad \mathrm{TDI}X(k_{ij}) = X^{k_{ij}}, \quad (22)$$

where k is again the rotation angle ($k = \eta, \varphi$). This allows us to write Eq. (21) as:

$$\delta X_{\rm corr} = \sum_{m=1}^{24} \delta C_{ijkl} (X^{k_{ij}} + X^{n^{\rm DWS}}). \quad (23)$$

As displayed in Eq. (23), this residual noise level is a result of the deviation of the estimated coefficient, δC_{ijkl}, multiplied with the jitter, $X^{k_{ij}}$, plus the sensing noise, $X^{n^{\rm DWS}}$.

A. Residual TTL noise

Since the simulated coupling coefficients are not perfectly recovered and the DWS sensing noise is added in the TTL estimation, we expect a remaining noise after subtracting TTL from the TDI outputs. The estimate of this residual noise and the consequent comparison to the other simulated noise sources is possible via the following sequence of steps:

(1) Generate a "noisy" set of data with all noise sources active, as in Sec. III, TTL noise included;
(2) Estimate TTL coefficients as in Sec. II B;
(3) Generate a set of data with only TTL noise active and use the DWS measurements [see Eq. (6)] simulated in Step 1;
(4) Subtract TTL from the dataset generated in Step 3 using TTL coefficient estimates of Step 2 and DWS measurements from Step 1.

The data presented in Sec. IV corresponds to the noisy dataset here. Thus, the MCMC results shown in Table I are used to subtract TTL as in Step 4. Figure 8 shows the results of this procedure. Here, the black line shows the TDI X output of the noisy dataset. It is the same as the black line in Fig. 7. $\check{X}$, shown in green in Fig. 8, represents the TDI X output in the configuration where TTL is the only noise source simulated (as in Step 3). As such, $\check{X}$ is a measurement of the true TTL coupling. The dashed red line ($\check{X}^{\rm TTL}$) indicates the respective TTL contribution in TDI, as the sum of 24 contributions as of Eq. (14), each of which is multiplied with the respective true coefficient. As a result, DWS sensing noise is included in the TTL estimation, $\check{X}^{\rm TTL}$, but not in $\check{X}$. Differently to Fig. 7, the TTL contribution, $\check{X}^{\rm TTL}$, is slightly above the TDI $\check{X}$ output of the respective dataset at frequencies below 0.2 mHz. This is due to the additional DWS sensing noise.

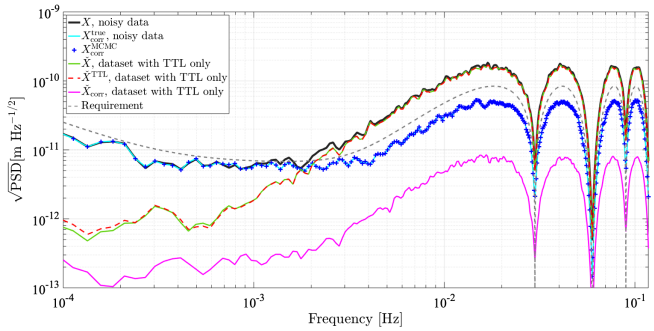

FIG. 8. Residual TTL noise after subtraction in terms of the square root of the PSD. This plot shows that the residual TTL noise, $\check{X}_{\rm corr}$, is significantly below the current estimate of the other noise sources. The full details are given in the text.

The residual TTL noise resulting from Step 4, meaning the result of subtracting the dashed red line from the green line, is depicted in magenta. We perform this subtraction using the estimated coefficient values reported in Table I and not the respective uncertainties. For comparison, we copied the two noise levels after TTL subtraction from Fig. 7. Again, the cyan line is the noise obtained when the true coefficient values are used to subtract TTL from the noisy dataset (simulated in Step 1), and it is compared with the noise level marked with the blue crosses, which is achieved when the MCMC results are used in the subtraction (as in Step 2). Let us now derive an expression for the magenta trace. Therefore, we indicate the dataset where TTL was the only noise source simulated with the symbol $\check{}$. Then, we have the correction as described in Step 4:

$$\check{X}_{\rm corr} = \check{X} - \sum_{m=1}^{24} (C_{ijkl} + \delta C_{ijkl}) \check{X}^{\rm TTL}_{C_{ijkl}}. \quad (24)$$

Using Eq. (22), we have for $\check{X}_{\rm corr}$:

$$\begin{aligned}\check{X}_{\rm corr} &= \check{X} - \sum_{m=1}^{24} (C_{ijkl} + \delta C_{ijkl}) \left(\check{X}^{k_{ij}} + \check{X}^{n^{\rm DWS}} \right) \\ &= \sum_{m=1}^{24} C_{ijkl} (\check{X}^{k_{ij}}) - \sum_{m=1}^{24} (C_{ijkl} + \delta C_{ijkl}) \left(\check{X}^{k_{ij}} + \check{X}^{n^{\rm DWS}} \right) \\ &= - \sum_{m=1}^{24} \delta C_{ijkl} \left(\check{X}^{k_{ij}} + \check{X}^{n^{\rm DWS}} \right) - \sum_{m=1}^{24} C_{ijkl} \check{X}^{n^{\rm DWS}}. \end{aligned} \quad (25)$$

Compared to Eq. (23), there is an additional term $\sum_{m=1}^{24} C_{ijkl} \check{X}^{n^{\rm DWS}}$ which explains the difference between the green trace in Fig. 7 and the magenta trace in Fig. 8.

The level of residual TTL noise is a few percent, in power, of the noisy TDI X data corrected with the true values (cyan trace in Fig. 8) at 0.01 Hz. Finally, it is visible in Fig. 8 that the remaining TTL noise is significantly below the other simulated noise sources. To be more explicit, the difference between the cyan and the magenta curve is due to the other noise sources except TTL present in the noisy dataset. These are mainly the residual acceleration noise on the TMs and other sensing noise sources in the interferometers.

V. DISCUSSION

This section explores how the accuracy in coefficient estimation depends on different noise levels and settings. Additionally, we want to investigate if the subtraction of TTL is still effective for these scenarios. We thus validate our procedure with one noise realization in the simulator for each case investigated. For clarity, we will only report the RMS accuracy over the 24 coefficients, as defined in Eq. (19). The noise levels taken into consideration are slight variations to the current design configuration (see Appendix B).

A. TTL coefficient values with drift

For our first investigation, we consider that the true TTL coefficients drift during a day. We then apply our methodology described in Sec. II B, which assumes constant coefficients values for the duration of the investigation. Thus, we aim to quantify the induced bias from this simplifying assumption to coefficient estimation. Based on current LISA modeling, we simulate a drift in the coupling coefficients of 0.15 mm/rad/day. So, the expected average value for each term will be $(2.3 + 0.075)$ mm/rad, which is half of the drift in a day. Figure 9 shows that the subtraction of TTL noise with the estimated constant coefficients is effective also when the simulated TTL coefficients actually drift in time. The RMS of the deviation

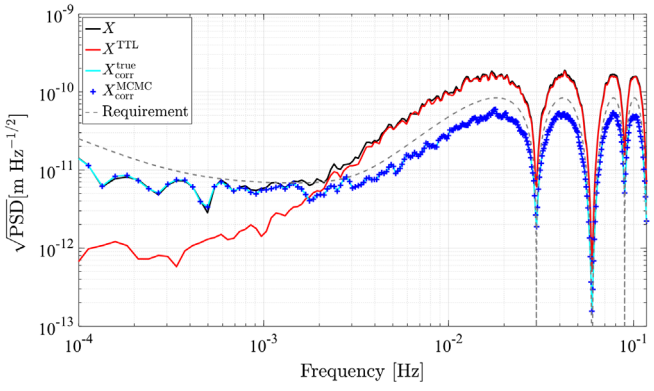

FIG. 9. TTL subtraction with drift in coefficient values in terms of the square root of the PSD. As visible, TTL noise (red) can be subtracted from TDI X (black) using the estimated values (blue crosses) at a level comparable to the case where perfect knowledge of the simulated values is assumed (cyan).

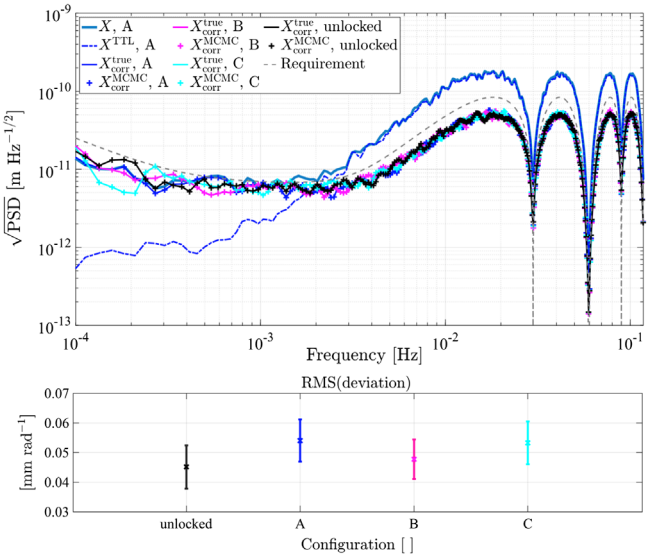

FIG. 10. Upper: TTL subtraction using the estimated coefficient values (crosses) is compatible to the subtraction using the true values (lines) for the different locking configurations tested. For comparison, TDI X (thick light blue curve) and TTL contribution to TDI (dash-dot blue trace) for the A locking configuration are also shown. Lower: RMS deviation estimated for the locking configurations as in the upper panel and without locking. The crosses indicate the RMS value of the deviation computed over the 24 coefficients and the error bar is the result from propagating the error of each coefficient deviation into the RMS.

of the coefficient values, as defined in Eq. (19), for this configuration is depicted in black in the lower panel of Fig. 10. As visible, the RMS coefficient accuracy satisfies the requirement of 0.1 mm/rad.

B. Laser locking configurations

The previous results showed that the TTL coefficients could be recovered with 0.1 mm/rad accuracy with the nominal configuration and the assumed drift. This test with drift did not consider laser locking. However, there are several ways to offset frequency-lock the six lasers on LISA. A possible realization is called a locking configuration. Here, we will focus on the three configurations shown in [19], but there exist more which are under study. To test the impact of the locking configurations on the accuracy of the estimated TTL coefficients and the subtraction efficiency, a dataset as in Sec. V A is simulated for each of the locking schemes A, B, C of [19] and then the 24 coefficients are estimated. Consequently, the expected 24 coefficient values would be 2.375 mm/rad. The results are collected in Fig. 10. As visible in the upper panel, TTL noise is subtracted to the level achieved when the simulated coefficient values are used in all the locking schemes taken into consideration, including the "unlocked" configuration with free-running lasers, which reflects the results of

Sec. VA. The RMS coefficient accuracy is below the requirement of 0.1 mm/rad in all cases, as shown in the lower panel of Fig. 10.

C. Random coefficient values with drift and random signs

In the previous test, the analysis was performed considering the same value for all the TTL coefficients and a single noise realization. To test the robustness of the subtraction procedure, we simulate 100 datasets with random coefficient values and signs. In more detail, we multiply a random value between -1 and 1, as generated from a uniform distribution, with 2.3 mm/rad. In addition, all the 24 coefficients are assumed to experience the same drift of (0.15 mm/rad/day). This test is done with the unlocked configuration only, although the performance is not expected to change based on the previous results. Figure 11 shows the histograms of the true coefficient values used in the 100 simulations. The TTL subtraction achieved using data from an example run is shown in the upper panel of Fig. 12. We observe a less dominant contribution of TTL to TDI above 4 mHz compared to the case of Fig. 7, for example. This is explained by the amplitude of the true coefficient values generated in this dataset, whose absolute values are smaller than the nominal value of 2.3mm/rad. Nevertheless, the coefficient estimation allows for an effective subtraction of TTL noise in TDI. The example run is representative of the 100 datasets in the sense that its RMS deviation is comparable to the RMS deviation of the other runs. This is shown in the lower panel of Fig. 12 which depicts the RMS deviation for each run. As visible, the achieved accuracy is within the requirement of 0.1 mm/rad for all the simulated datasets. For comparison, the result of Sec. VA, namely from taking the nominal values with constant drift for all the coefficients, is added in black. We show the histogram of the RMS deviation of the 100 runs on the right. The mean of the RMS deviation is (0.040 ± 0.001) mm/rad.

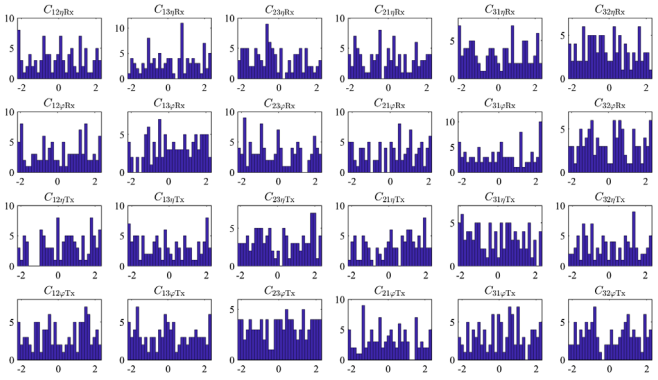

FIG. 11. Histograms of the true coefficient values in mm/rad used in the 100 simulations.

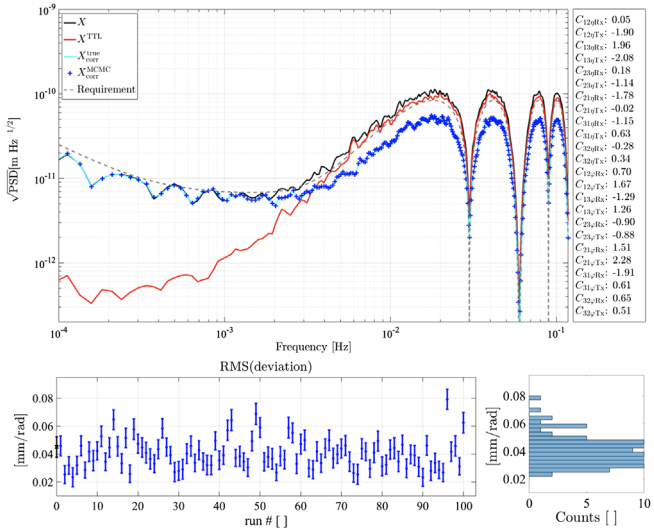

FIG. 12. Upper: TTL subtraction with random coefficient values, constant drift and random signs for the run #10 in terms of the square root of the PSD. The true values are reported in the box next to the figure with units of mm/rad. Lower: Left: RMS deviation for each of the 100 simulated datasets. For comparison, the result of in Sec. VA is added in black. Lower panel: Right: histogram of the RMS deviations.

D. Varying TTL noise level

The nominal configuration assumes that all the 24 coefficients have the same value of 2.3 mm/rad. In this section, we explore a possible impact on the coefficient accuracy and the subtraction efficiency arising from all the coefficients having the same value but this value is now different to the nominal one. More specifically, we consider two example cases: The first case assumes low TTL noise ($C_{ijkl} = 1$ mm/rad), and the second case deals with exceptionally high TTL noise ($C_{ijkl} = 10$ mm/rad). For this investigation, the configuration with free-running lasers is implemented in the simulator. The results of this test are summarized in Fig. 13. We show the estimated contribution of TTL noise to TDI X, as dashed lines, for three selected example values for all of the 24 TTL coefficients. The solid traces represent the subtraction of these contributions from raw TDI X (not shown for clarity) using the true coefficient values. The subtraction using the estimated coefficient values is indicated with the crosses. For comparison, the figure includes the results from setting all TTL coefficients to 2.3 mm/rad (black trace), corresponding to the nominal configuration as of Sec. IV.

As expected, the TTL contribution in Fig. 13 scales with the TTL coefficient level across the investigated frequency band. In all cases, the subtraction using the estimated coefficients is comparable to the result using the true coefficients. We note that the subtraction result for the case of TTL $= 10$ mm/rad remains above the subtraction result of the other two cases. This is because according to our linear model using the satellite telemetry [see Eq. (6)],

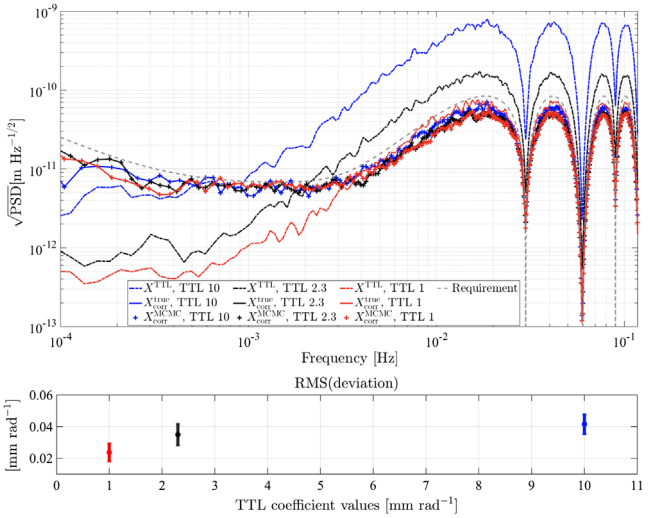

FIG. 13. Upper: TTL contribution to TDI X and corrected spectra for example cases of TTL noise at different levels as indicated in the legend with units of mm/rad for all 24 coefficients. Lower: RMS deviation for the different TTL levels as in the upper panel.

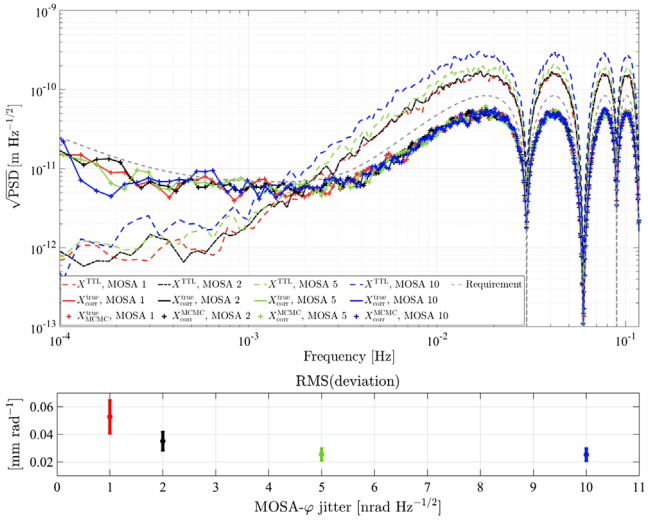

FIG. 14. Upper: TTL contribution to TDI X and corrected spectra for the example cases of MOSA-φ jitter. Lower: RMS deviation for the example cases of MOSA-φ jitter.

the TTL coefficient multiplies the jitter and the additive sensing noise. Since we are looking at the subtraction result between TDI X and the estimated TTL contributions, the jitter is common to both and therefore subtracts. However, the angular sensing noise is only part of the estimated TTL contribution. Therefore, in this case, it provides an addition to the longitudinal interferometer sensing noise, which was found to limit the result after the subtraction of TTL. However, the lower panel of Fig. 13 demonstrates that the average accuracy is within the required level. Nonetheless, it seems to decrease toward higher TTL coefficient values.

E. Varying MOSA-φ angular jitter level

In this section, we investigate a possible change in coefficient accuracy when we simulate other levels of MOSA-φ jitter than the nominal one (see Appendix B), while the SC-φ jitter remains constant. Thus, we only vary a part of the jitter displayed in Eq. (4). In this test, we set the MOSA-φ jitter levels at 0.01 Hz to three different values: 1, 5, and 10 nrad/$\sqrt{\text{Hz}}$. This test is performed with the unlocked configuration and the nominal constant value of 2.3 mm/rad for all 24 coefficients. We present the results in Fig. 14 and maintain the style of Fig. 13. Indeed, the black trace and dots are the same nominal results in both of these plots. Similar to the results of Sec. V D and as expected, the TTL contribution scales with the level of MOSA-φ jitter. As visible in the upper panel of Fig. 14, the subtraction of TTL noise is effective in all cases, and the average accuracy of the respective estimated coefficients fulfills the requirement, as shown in the lower panel. In particular, the accuracy increases with larger MOSA-φ jitter until 5 nrad/$\sqrt{\text{Hz}}$ since this jitter can be considered as a part of the signal for TTL coefficient estimation. One of the limiting factors on the accuracy is the DWS noise.

F. Varying DWS sensing noise level

As discussed in Sec. IV A, the DWS sensing noise is a driver of both the parameter estimation accuracy and the efficiency of the subtraction. Therefore, we explore it in more detail in this section. As in Sec. V D, this exploration neglects phase-locking and uses the nominal constant value for all 24 TTL coefficients.

In the upper panel of Fig. 15 we show the subtraction results for some DWS levels above and below the nominal one (see Appendix B). We express these levels in terms of the square root of the PSD and relative to the inertial space. This time, we do not show the full spectra as in previous figures but the square root of the averaged PSD around 0.01 Hz. More specifically, this average is applied to TDI X corrected with true ($X^{\text{true}}_{\text{corr}}$) and estimated values ($X^{\text{MCMC}}_{\text{corr}}$). For comparison, we include the requirement on TDI X as in Fig. 2 averaged around the same frequency. As visible, for DWS noise levels from 0 to approximately 0.3 nrad Hz$^{-1/2}$, the subtraction result reaches the same noise level around 30 pm/$\sqrt{\text{Hz}}$ to within the errors. This noise level is reached both in the case of using the true and the estimated coefficients. No difference between the corresponding data points is discernible.

For the DWS sensing noise levels between 0.5 and 1 nrad Hz$^{-1/2}$, we note that the noise level of the corrected data is above the 30 pm/$\sqrt{\text{Hz}}$. Accordingly, the subtraction is less effective in this range due to the increased DWS sensing noise. Here, no difference between the coefficients used for the correction can be identified. In other words, the cyan and blue data points agree very well. This implies that

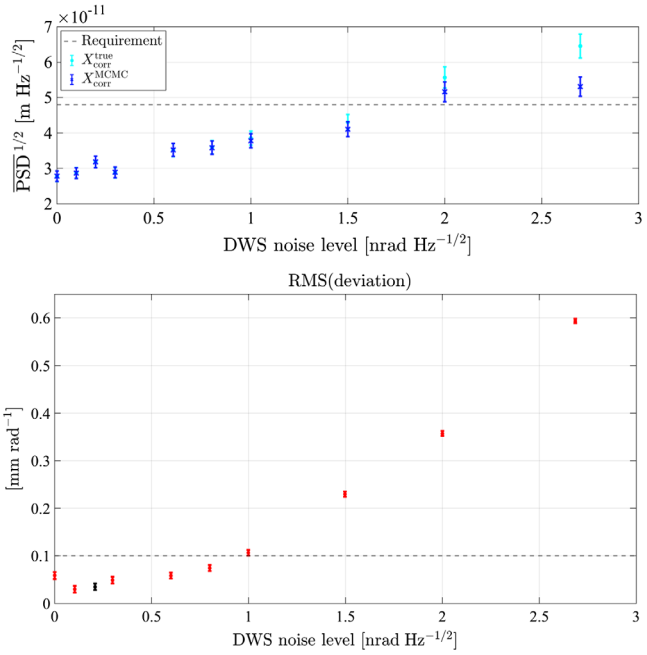

FIG. 15. Upper: Square root of the PSD averaged around 0.01 Hz of TDI X corrected with true ($X^{\mathrm{true}}_{\mathrm{corr}}$) and estimated values ($X^{\mathrm{MCMC}}_{\mathrm{corr}}$) for different DWS noise levels. The dashed line indicates the requirement on TDI X after TTL subtraction averaged around 0.01 Hz. Lower: RMS deviation for the same DWS levels as in the upper panel. The case of the nominal configuration with DWS noise of 0.2 nrad $\mathrm{Hz}^{-1/2}$ is depicted in black. The results are compared to the required accuracy indicated by the dashed line.

the limit of the subtraction is the sensing noise here and not the coefficient estimation. Let us now consider the DWS sensing noise levels from 1.5 to 2.67 nrad $\mathrm{Hz}^{-1/2}$. Here we see that the noise level of the corrected data is increasing, and so is the discrepancy between the correction using the true and the estimated values. It seems likely that the noise level is lower when the estimated coefficients are used because the minimization yields the optimal coefficients to minimize the total noise and thus overestimates the TTL contribution. Further investigations will be done to explore this behavior. To conclude, we find that the subtraction is very effective for DWS sensing noise below 0.5 nrad $\mathrm{Hz}^{-1/2}$, where the TDI output is reduced to approximately 30 pm $\mathrm{Hz}^{-1/2}$ compared to a reduction only to 65 pm $\mathrm{Hz}^{-1/2}$ for the case of DWS equal to 2.67 nrad $\mathrm{Hz}^{-1/2}$ which exceeds the requirement.

In the lower panel of Fig. 15, we show the RMS accuracy of the estimated coefficient values. It is within the required accuracy of 0.1 mm/rad, indicated by the dashed line, for DWS noise levels from 0 to approximately 0.8 nrad $\mathrm{Hz}^{-1/2}$. However, when the nominal DWS noise increases by a factor of five or more, the RMS deviation is above the requirement. The reason for this lies in the level of DWS noise itself which is added in TTL estimation, according to Eq. (6). The violation of the requirement is more evident when DWS noise reaches 2.67 nrad $\mathrm{Hz}^{-1/2}$ where the parameter estimation becomes troublesome.

VI. CONCLUSIONS

TTL noise is expected to be a major noise source in the LISA ISI. While it shall be minimized by the design, construction, and integration of the SC and via the beam alignment mechanism, the remaining noise has to be subtracted in postprocessing. In this paper, we have shown a possible solution that does not reduce the science measurement time of the observatory. This solution relies on noise minimization and uses the DWS measurements to estimate the TTL contribution.

We used a LISA simulator to validate the noise minimization approach. This simulator includes the relevant noise sources for this analysis and their levels are based on the current knowledge (see Appendix B). Accordingly, we report results obtained from specific noise models and realizations. When we apply our approach to the thus simulated data, we can estimate the TTL coefficients with an accuracy of better than ± 0.1 mm/rad. This allows us to subtract the induced TTL noise such that the remainder is below the current estimate of the other noise sources. We identified correlation among the 24 TTL coefficients of our model. It is driven by the relative levels of SC and MOSA jitter and the fact that two MOSAs share the same SC. More detailed investigations will follow.

We generated data with different noise level settings and applied the same procedure to validate it more profoundly. In the first test, we assumed a constant drift over one day. The second test considered the frequency locking of the six lasers of the constellation. In a third test, we checked the procedure on 100 datasets where all 24 TTL coefficients had different random values and signs. These 100 datasets revealed no systematic problems with the procedure. The RMS of the deviations to the true TTL coefficient level is below the required accuracy of 0.1 mm/rad for all datasets. We could validate the TTL subtraction for an example. Two other tests showed that the TTL coefficient level and the angular jitters were driving the TTL contribution level. In particular, while an increase in the MOSA-φ jitter level simplified the estimation of the TTL contribution, an increase of the TTL coefficient values also introduced more angular sensing noise and thus did rather decrease the RMS TTL coefficient estimation accuracy. In the last test, we varied the angular sensing noise. We found an RMS accuracy below 0.1 mm/rad with the DWS sensing noise increased by up to a factor of 4. We found that the DWS noise either directly or via increased TTL coefficient amplitudes, can decrease the accuracy of the estimated coefficients when it becomes significantly larger than expected. However, all of these five tests increased the confidence in the noise minimization procedure.

VII. OUTLOOK

Possible limits of this approach. Evidently, this approach only works as long as the TTL noise is the dominating noise source in the TDI output in a given frequency range. If the optical bench and telescope construction and MOSA assembly exceeded expectations, TTL noise would already be minimized in hardware to a level that makes it indistinguishable from the other noises in the TDI outputs. In this case, the presented approach would be obsolete. If other noise sources dominated, the determination of the TTL coefficients would be difficult until these other noise sources would have been eliminated.

An additional limitation is that we currently use a model of the expected noise without TTL to whiten the data during the estimation process. Should a usable noise model not be available, this process could be adapted to use iterative whitening, starting with a guess at the noise model and then taking the model parameters from the minimization.

The third category of limitations of this method concerns the availability of data. In the examples presented, we have used approximately 24 hrs of uninterrupted data without glitches or any nonstationarities. We would expect to find a degradation of the reported performance in case of data gaps and nonstationary noise behavior. This could be even worse in the extreme case of a lost arm when only one of the three Michelson combinations could be formed. In this case, we would no longer obtain the reported results since we combine all three Michelson combinations to estimate the coefficients. Even though we would not need to estimate 24 coefficients in this case because those related to the nonoperating arm would be irrelevant, the efficiency of the subtraction procedure might be limited due to the coefficient correlations. These questions could not be studied in detail in this mission phase yet.

Additionally, with significantly higher drifts, we expect that the TTL estimation model will also need to include a model of the drift. On the contrary, should the true drift be significantly below the current estimates, we could apply the linear model to an extended period of data. Without additional interruptions, we expect a longer duration to increase the accuracy of the estimated coefficients.

Possible improvements of this approach. Apart from addressing the above limitations where possible, let us mention that if the noise shapes confirm this, extending the frequency range used for the fit to higher frequencies is possible. One likely issue will be the presence of gravitational wave signals, especially the galactic binary foreground, but more investigation is needed. Individual gravitational wave signals should not be affected in their amplitude or frequency by this TTL subtraction procedure, nor should they deteriorate the efficiency of the subtraction. Detailed investigations are planned as future work. In addition, using the TDI cross spectra, XY, YZ, and XZ could be investigated. Another combination of interest could be the ζ combination [21], as well as other more recent combinations [22], which can be used to characterize TTL noise in the absence of strong gravitational wave signals. We will explore other combinations in a further publication.

Moreover, in this proof-of-principle activity, we have studied the TTL coefficient estimation and the noise subtraction for 24 hrs of data, intending to enable quick alerts for gravitational wave sources or routine performance monitoring. In the future, this method could also be applied iteratively, which means as part of a global fit, which identifies all gravitational wave signal content.

Possible design of in-orbit calibration maneuvers. The current thinking is to develop a calibration maneuver as a backup solution in the event of difficulties with the approach presented so far. Such maneuvers have also been performed on LISA's technology demonstrator mission LISA Pathfinder [4,23,24]. Center-of-mass maneuvers on a different satellite mission with intersatellite interferometry have been used to characterize TTL coupling, see [25]. However, many aspects would have to be considered in the design of such a calibration maneuver for LISA, which is also discussed in [10]. One aspect concerns the available torque authorities on the SC and the MOSA, see [26]. This work could be extended by considering the closed-loop control and its transfer function. In addition, the dependency of the DWS noise on the angular offsets and the TDI transfer function should be considered. That means avoiding frequencies at the dips around multiples of 0.03 Hz (see for example Fig. 2) to obtain a good signal-to-noise ratio. Moreover, we recommend carefully checking for cross-couplings to other degrees of freedom, for example, via stiffnesses or actuation cross-talks.

ACKNOWLEDGMENTS

S. P., R. G., M. H., G. W., and G. H. gratefully acknowledge support by Deutsches Zentrum für Luft- und Raumfahrt (DLR) with funding of the Bundesministerium für Wirtschaft und Energie with a decision of the Deutsche Bundestag (DLR Project Reference No. FKZ 50 OQ 11801). N. K. acknowledges the support from the Gr-PRODEX 2019 funding program. E. F. gratefully acknowledges support from the UK Space Agency.

APPENDIX A: ANALYTICAL MODELS OF A, E AND T AND SIMULATION VALIDATION

As described in Sec. II B, we whiten the noise using a current estimate of the expected noise in TDI without the TTL contribution. This means we set TTL noise to 0 in this calculation. The analytic model of such a predicted noise in TDI A, E, and T derives from symbolic time-domain beam equations. More specifically, we calculate TDI for six unequal but static LISA links, assuming only the main noise sources present and no signals. These noise sources are the sensing noise of each interferometer and the residual acceleration noise on a single TM. Additionally, the fiber

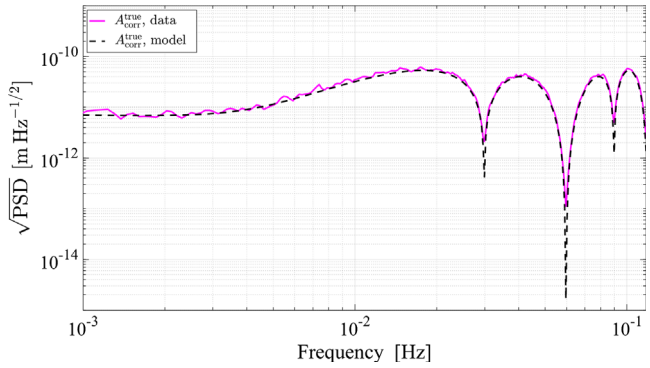

FIG. 16. Comparison between data and model for A combination after TTL subtraction using true coefficient values.

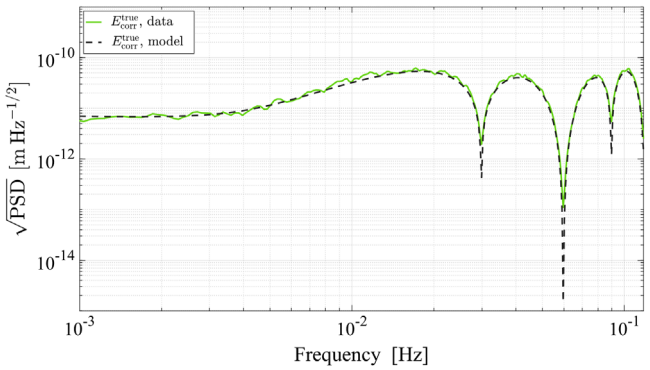

FIG. 17. Comparison between data and model for E combination after TTL subtraction using true coefficient values.

noise is included. This is the noise arising from the optical fibers between the two OBs on the same SC. In the last step of the calculation, we set all of the noise sources mentioned above to the noise levels as specified in Appendix B. The resulting models for unequal arms are used in the analysis, and are shown in Figs. 16–18, but the corresponding expressions are too long to reproduce here. However, they are rather similar to the case of assuming the same length for all the arms. Therefore, we reproduce the expressions for equal arms here:

$$\begin{aligned}S_A(f) &= S_E(f)\\ &= (2\mathcal{D}^8 + 4\mathcal{D}^7 + 8\mathcal{D}^6 - 4\mathcal{D}^5 - 24\mathcal{D}^4 - 12\mathcal{D}^3 - 8\mathcal{D}^2 + 12\mathcal{D} + 2\bar{\mathcal{D}}^8 + 4\bar{\mathcal{D}}^7 + 8\bar{\mathcal{D}}^6 - 4\bar{\mathcal{D}}^5\\ &\quad - 24\bar{\mathcal{D}}^4 - 12\bar{\mathcal{D}}^3 - 8\bar{\mathcal{D}}^2 + 12\bar{\mathcal{D}} + 44)\cdot S_{\text{acc}} + (\mathcal{D}^7 + 4\mathcal{D}^6 - \mathcal{D}^5 - 8\mathcal{D}^4 - 3\mathcal{D}^3 - 4\mathcal{D}^2\\ &\quad + 3\mathcal{D} + \bar{\mathcal{D}}^7 + 4\bar{\mathcal{D}}^6 - \bar{\mathcal{D}}^5 - 8\bar{\mathcal{D}}^4 - 3\bar{\mathcal{D}}^3 - 4\bar{\mathcal{D}}^2 + 3\bar{\mathcal{D}} + 16)\cdot S_{\text{s}} + (\mathcal{D}^8/2 + \mathcal{D}^7 + 2\mathcal{D}^6 - \mathcal{D}^5 - 6\mathcal{D}^4 - 3\mathcal{D}^3\\ &\quad - 2\mathcal{D}^2 + 3\mathcal{D} + \bar{\mathcal{D}}^8/2 + \bar{\mathcal{D}}^7 + 2\bar{\mathcal{D}}^6 - \bar{\mathcal{D}}^5 - 6\bar{\mathcal{D}}^4 - 3\bar{\mathcal{D}}^3 - 2\bar{\mathcal{D}}^2 + 3\bar{\mathcal{D}} + 11)\cdot S_{\text{e}}\\ &\quad + (\mathcal{D}^7 + 4\mathcal{D}^6 - \mathcal{D}^5 - 8\mathcal{D}^4 - 3\mathcal{D}^3 - 4\mathcal{D}^2 + 3\mathcal{D} + \bar{\mathcal{D}}^7 + 4\bar{\mathcal{D}}^6 - \bar{\mathcal{D}}^5 - 8\bar{\mathcal{D}}^4 - 3\bar{\mathcal{D}}^3\\ &\quad - 4\bar{\mathcal{D}}^2 + 3\bar{\mathcal{D}} + 16)\cdot S_{\text{t}} + (2\mathcal{D}^6 - \mathcal{D}^8/2 - 2\mathcal{D}^4 - 2\mathcal{D}^2 - \bar{\mathcal{D}}^8/2 + 2\bar{\mathcal{D}}^6 - 2\bar{\mathcal{D}}^4 - 2\bar{\mathcal{D}}^2 + 5)\cdot S_{\mu},\end{aligned} \tag{A1}$$

$$\begin{aligned}S_T(f) &= (2\mathcal{D}^8 - 8\mathcal{D}^7 + 8\mathcal{D}^6 + 8\mathcal{D}^5 - 24\mathcal{D}^4 + 24\mathcal{D}^3 - 8\mathcal{D}^2 - 24\mathcal{D} + 2\bar{\mathcal{D}}^8 - 8\bar{\mathcal{D}}^7 + 8\bar{\mathcal{D}}^6 + 8\bar{\mathcal{D}}^5\\ &\quad - 24\bar{\mathcal{D}}^4 + 24\bar{\mathcal{D}}^3 - 8\bar{\mathcal{D}}^2 - 24\bar{\mathcal{D}} + 44)\cdot S_{\text{acc}} + (4\mathcal{D}^6 - 2\mathcal{D}^7 + 2\mathcal{D}^5 - 8\mathcal{D}^4 + 6\mathcal{D}^3 - 4\mathcal{D}^2\\ &\quad - 6\mathcal{D} - 2\bar{\mathcal{D}}^7 + 4\bar{\mathcal{D}}^6 + 2\bar{\mathcal{D}}^5 - 8\bar{\mathcal{D}}^4 + 6\bar{\mathcal{D}}^3 - 4\bar{\mathcal{D}}^2 - 6\bar{\mathcal{D}} + 16)\cdot S_{\text{s}} + (\mathcal{D}^8/2 - 2\mathcal{D}^7 + 2\mathcal{D}^6 + 2\mathcal{D}^5 - 6\mathcal{D}^4 + 6\mathcal{D}^3\\ &\quad - 2\mathcal{D}^2 - 6\mathcal{D} + \bar{\mathcal{D}}^8/2 - 2\bar{\mathcal{D}}^7 + 2\bar{\mathcal{D}}^6 + 2\bar{\mathcal{D}}^5 - 6\bar{\mathcal{D}}^4 + 6\bar{\mathcal{D}}^3 - 2\bar{\mathcal{D}}^2 - 6\bar{\mathcal{D}} + 11)\cdot S_{\text{e}}\\ &\quad + (4\mathcal{D}^6 - 2\mathcal{D}^7 + 2\mathcal{D}^5 - 8\mathcal{D}^4 + 6\mathcal{D}^3 - 4\mathcal{D}^2 - 6\mathcal{D} - 2\bar{\mathcal{D}}^7 + 4\bar{\mathcal{D}}^6 + 2\bar{\mathcal{D}}^5 - 8\bar{\mathcal{D}}^4 + 6\bar{\mathcal{D}}^3\\ &\quad - 4\bar{\mathcal{D}}^2 - 6\bar{\mathcal{D}} + 16)\cdot S_{\text{t}} + (2\mathcal{D}^6 - \mathcal{D}^8/2 - 2\mathcal{D}^4 - 2\mathcal{D}^2 - \bar{\mathcal{D}}^8/2 + 2\bar{\mathcal{D}}^6 - 2\bar{\mathcal{D}}^4 - 2\bar{\mathcal{D}}^2 + 5)\cdot S_{\mu},\end{aligned} \tag{A2}$$

where $\bar{\mathcal{D}}$ indicates the complex conjugate of the delay operator $\mathcal{D}$ which here is assumed to be the same for all the arms. More explicity, $\mathcal{D}$ is a complex quantity and here it is equal to $\exp(-i2\pi fL/c)$ with L as the length of a LISA arm. The terms S_{acc}, S_{s}, S_{e}, S_{t} and S_{μ} indicate respectively the single TM acceleration noise, the sensing noise in the ISI, TM and reference interferometer and the fiber noise expressed in PSD terms. Accordingly, $S_A(f)$, $S_E(f)$ and $S_T(f)$ are the PSD of A, E and T.

Figures 16–18 show an example comparison between the data (nominal configuration, see Appendix B) and the analytical model for unequal arms in terms of the square root of the PSD. The data is shown after TTL has been subtracted using the true coefficient values and is therefore consistent with the model of TDI A, E, and T, which assumes no TTL present. As visible, the data agree with the model in all cases.

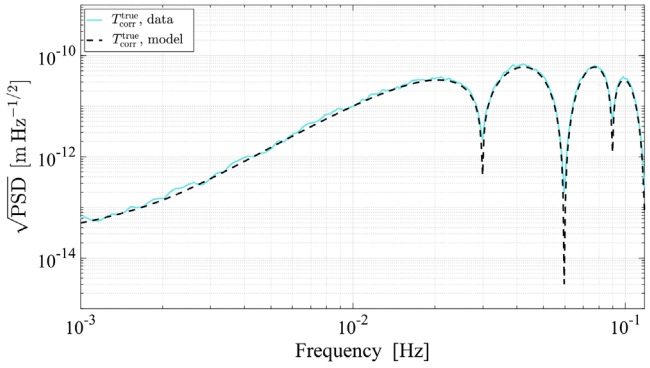

FIG. 18. Comparison between data and model for T combination after TTL subtraction using true coefficient values.

APPENDIX B: NOMINAL CONFIGURATION SETTINGS

Table II provides a list of the most important parameters that describe the presented nominal configuration, as used for the results of Fig. 7. For each noise entry, we report the respective value at 0.01 Hz, expressed in terms of the square root of the PSD and the parameters of the frequency shape. We implement the noise sources using a pole/zero model object in LTPDA [18]. The LTPDA AO constructor takes a defined pole/zero model and generates random noise with the prescribed spectral shape. The process is based on an algorithm described in [27].

TABLE II. Simulation parameters for the nominal configuration.

Parameter	Value
SC jitter η (w.r.t. inertial space)	5 nrad/$\sqrt{\text{Hz}}$
SC jitter φ (w.r.t. inertial space)	5 nrad/$\sqrt{\text{Hz}}$
SC jitter θ (w.r.t. inertial space)	5 nrad/$\sqrt{\text{Hz}}$
Frequency shape	Gain: $(0.8\times10^{-3}/1\times10^{-8})^2$ Poles: $\{1\times10^{-8}, 1\times10^{-8}, 1\}$ Zeros: $\{0.8\times10^{-3}, 0.8\times10^{-3}\}$
MOSA jitter η (w.r.t. SC)	1 nrad/$\sqrt{\text{Hz}}$
MOSA jitter φ (w.r.t. SC)	2 nrad/$\sqrt{\text{Hz}}$
Frequency shape	Gain: $(0.8\times10^{-3}/1\times10^{-8})^2$ Poles: $\{1\times10^{-8}, 1\times10^{-8}, 1\}$ Zeros: $\{0.8\times10^{-3}, 0.8\times10^{-3}\}$
DWS sensing noise along η, φ (at the QPR[a])	70 nrad/$\sqrt{\text{Hz}}$
Magnification factor	335
Frequency shape	Gain: $(2\times10^{-3}/1\times10^{-6})^2$ Poles: $\{1\times10^{-6}, 1\times10^{-6}, 8, 8\}$ Zeros: $[2\times10^{-3}1/\sqrt{2}]$[b]
TM force noise	4.6 fN/$\sqrt{\text{Hz}}$
Frequency shape	Gain: $(3\times10^{-4}/5\times10^{-6})$ Poles: $\{5\times10^{-6}, 1\}$ Zeros: $\{3\times10^{-4}\}$
ISI sensing noise	6.35 pm/$\sqrt{\text{Hz}}$
Frequency shape	Gain: $(2\times10^{-3}/1\times10^{-6})^2$ Poles: $\{1\times10^{-6}, 1\times10^{-6}, 8, 8\}$ Zeros: $[2\times10^{-3}1/\sqrt{2}]$
TM IFO[c] sensing noise	1.42 pm/$\sqrt{\text{Hz}}$
Frequency shape	Gain: $(2\times10^{-3}/1\times10^{-6})^2$ Poles: $\{1\times10^{-6}, 1\times10^{-6}, 8, 8\}$ Zeros: $\{2\times10^{-3}, 2\times10^{-3}\}$
Reference IFO sensing noise	3.32 pm/$\sqrt{\text{Hz}}$
Frequency shape	Gain: $(2\times10^{-3}/1\times10^{-6})^2$ Poles: $\{1\times10^{-6}, 1\times10^{-6}, 8, 8\}$ Zeros: $[2\times10^{-3}1/\sqrt{2}]$
Fiber noise	3 pm/$\sqrt{\text{Hz}}$
Frequency shape	White noise
Laser frequency noise	300Hz/ $\sqrt{\text{Hz}}$
Frequency shape	Gain: $(2\times10^{-3}/2\times10^{-5})^2$ Poles: $\{2\times10^{-5}, 2\times10^{-5}, 9, 9\}$ Zeros: $\{2\times10^{-3}, 2\times10^{-3}\}$

[a]Quadrant Photo-Receiver.
[b]The second argument in the [brackets is the quality factor of the zero.
[c]Interferometer.

APPENDIX C: EXAMPLE PROPAGATION OF TTL COUPLING

In this section, we illustrate the propagation of the TTL-induced phase change. For this purpose, we simulate a single pulse with the shape of a sine wave to occur in MOSA 31 along the φ degree of freedom. The pulse has an amplitude of 1 μm, a frequency of 1 Hz, and lasts for 1 s.

Let us begin with a broader view in Sec. C 1. Simulation results for a single pulse in a more realistic noise configuration will be shown and described in Sec. C 2.

1. Overview of TTL noise propagation

Figure 19 provides a strongly simplified sketch of the TTL propagation and subtraction. For simplicity, we assume that all other MOSAs and all 3 SC are perfectly quiet. Moreover, we ignore the sign of the interferometer measurements and all other noise sources except TTL. Most importantly, ignoring laser frequency noise allows the TTL noise to be directly discernible in the ISI measurements, while in reality, laser frequency noise dominates. Moreover, we do not consider the impact of a closed-loop satellite control scheme and its reactions to this pulse for

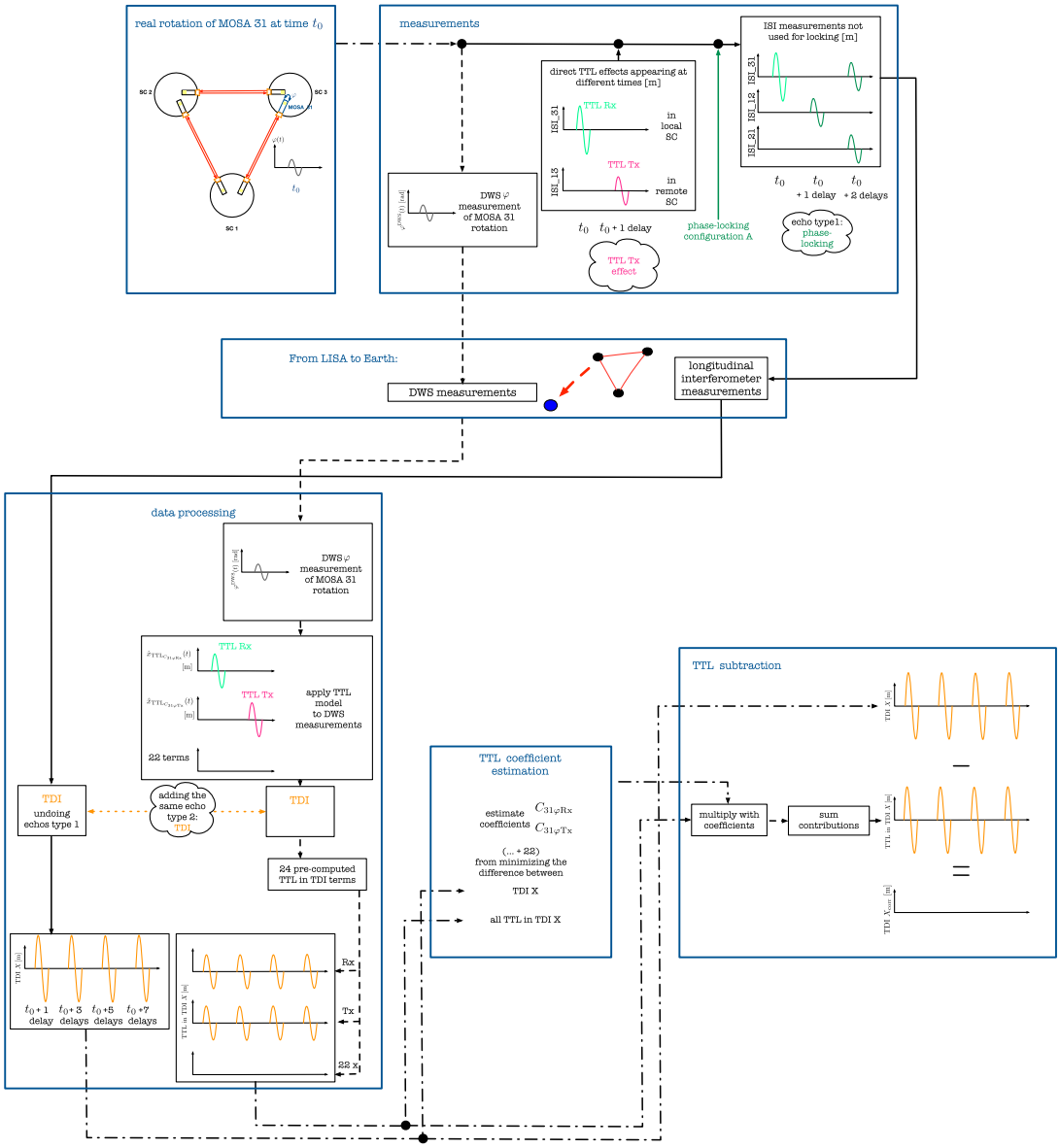

FIG. 19. Schematic overview of TTL noise propagation, coefficient estimation and TTL subtraction. The solid lines indicate the longitudinal interferometer measurements, while the dashed lines refer to the DWS measurements. The combined or otherwise processed measurements are drawn as dash-dot lines. A full description including the underlying assumptions is given in the text.

simplicity. In addition, the phase-locking is assumed to work perfectly. This diagram only considers the output of TDI X as an example but the coefficient estimation uses A, E and T (as described in Sec. II B).

In Fig. 19, we begin on the top left with a single pulse on MOSA 31 along φ at a time t_0. This true rotation is then measured, as explained in the top right box. Indeed, the DWS φ channel measures this rotation. In addition, the rotation leads to TTL noise in the longitudinal measurements. This happens simultaneously with the original rotation for the Rx TTL and one light travel time along the arm later in the remote SC for the Tx TTL. In this example, we assume, for simplicity, the TTL Rx component to be larger than the TTL Tx component. The longitudinal ISI measurements are, however, also subject to phase-locking. The ISI measurements will look differently depending on the MOSA jittering and the respective locking scheme. Here, we show locking scheme A as an example.

So far, we have illustrated what will happen inside the LISA satellites. Note that, on Earth, only the DWS measurement of the rotation and the longitudinal interferometer measurements will be available, not the true rotation itself. The box in the center of the picture illustrates the downlink of the data.

On Earth, there will be several steps of data processing. Let us begin with the processing of the DWS measurements. In the first of these steps, we estimate the TTL contribution from the measured φ jitter. In this example,

when only MOSA 31 is rotating, we obtain two phase noise contributions converted to a length from Eq. (12). The other 22 terms will be vanishing. Next, we apply TDI to each of these 24 contributions to obtain 24 precomputed TTL in TDI terms. Similarly, TDI is applied to the longitudinal measurements. TDI introduces the same type of echos in both cases due to the applied delays. Since TDI also removes the echos type 1 introduced by the phase-locking, the resulting time series of TDI X and TTL in TDI X show the same echos at the same times. For this particular example, we find echos at times $t_0 + 1$ delay, $t_0 + 3$ delays, $t_0 + 5$ delays, $t_0 + 7$ delays. Here, a delay equals the light travel time between two SC, which we assume is identical for all arms.

After the data processing, the TTL coefficients can be estimated by minimizing the difference between TDI X and the sum of all TTL in TDI X terms. In a more realistic scenario, the implementation described in Sec. II B can be used. In principle, the TTL coefficients can also be obtained from alternative methods, leaving the remainder of the procedure unaffected.

Let us proceed with the TTL subtraction, which is illustrated in the box on the bottom right. The TTL contribution in TDI now results from combining the estimated coefficients with the precomputed TTL in TDI terms and then summing up all the 24 terms. We note that the echos have the same amplitude as the TDI X data in this case of correctly estimated coefficients. The TDI X is directly obtained from the data processing step. TTL is finally removed by subtracting these two time series. Since no other MOSA or SC is jittering in this example, the difference between the two is vanishing.

2. Simulation of TTL noise propagation

In the previous paragraph, we have given a broader overview of the propagation of our example pulse in MOSA 31. In this section, we will explain the echos of this pulse due to the phase-locking in a more realistic noise configuration and present the corresponding simulation results.

We use the simulation configuration described in Appendix B with three exceptions to help the visualization. One of these is that the laser frequency noise is ignored for this test which makes the TTL in the intersatellite interferometers discernible. Another difference is that the amplitude of the TTL coefficients is 3 mm/rad for the Rx coefficients and 2 mm/rad for the Tx coefficients. With this change, we can distinguish by eye the propagation of the injected pulse along the Rx and Tx paths. In the nominal configuration, we assume no laser locking, but here we choose the locking scheme A (see Sec. V B and [19]) to show how the locking results in the propagation of the pulse.

For clarity, this locking scheme is depicted in Fig. 20. In this scheme, the local laser with respect to MOSA 32 is frequency stabilized using a cavity and acts as the primary

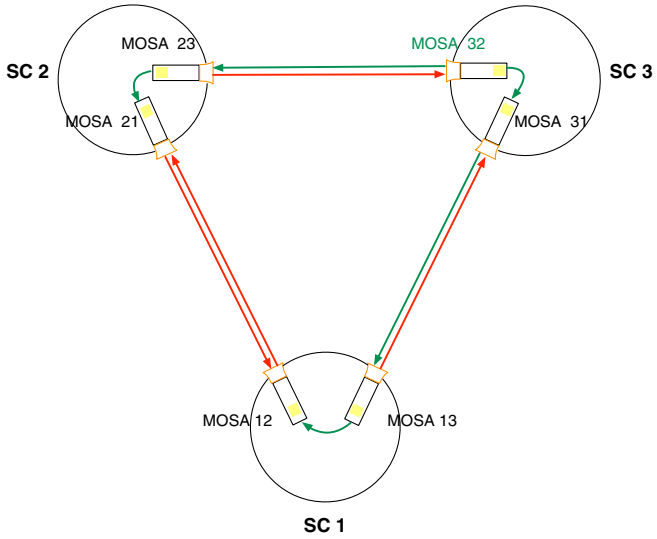

FIG. 20. Illustration of locking scheme A. The laser 32 is used as the primary laser. The arrows marked in green indicate the interferometric measurements used to transponder-lock the other five lasers.

laser. The other lasers are transponder-locked to this one using the ISI and reference interferometer signals. This is illustrated by the green arrows in Fig. 20. For example, laser 23 is locked using the ISI 23 to laser 32. For the locking, only the longitudinal measurements are used and therefore, the locking does not link the jitter of one MOSA to the angular measurements on other MOSAs. Figure 21 shows the ISI outputs for this simulation. Since the simulator assumes perfect locking, the ISI 13 and 23 measurements are zero and therefore not shown. We can see the original pulse at the injection time (∼382 s) in the ISI 31 output. Since the local MOSA 31 jitter multiplies the Rx coefficient, the pulse amplitude is the largest of the four. Delayed by the light travel time along the arm, the pulse appears in the form of three echos in several ISI measurements. More specifically, it reappears first in ISI 12 since

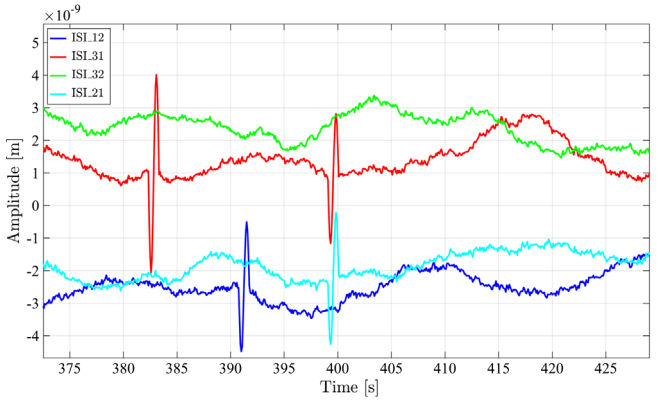

FIG. 21. ISI outputs after removal of linear trend and converted to meter for the simulation of a pulse as described in the text. We can see the original pulse in the ISI 31 output and the echos due to the locking scheme.

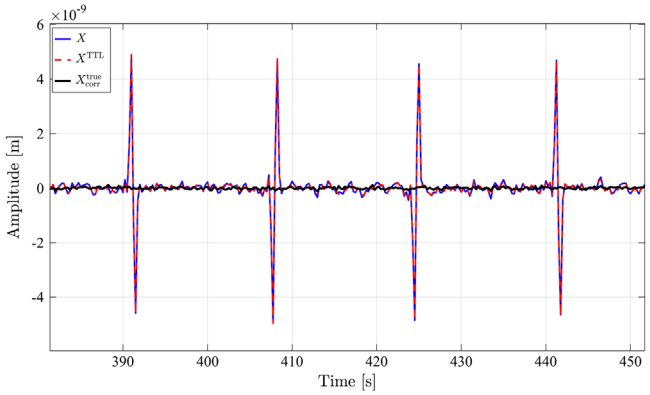

FIG. 22. Time series of TDI X, TTL in TDI computed using the true coefficient values and their difference for the simulation described in the text.

laser 12 is locked to laser 13 and laser 13 is locked to laser 31 via the ISI 13, which measures the pulse delayed by the light travel time. The amplitude of this echo is smaller than the amplitude of the original pulse since it results from multiplying the initial pulse by the Tx coefficient. Since the pulse is imprinted onto the beam from SC 1 to SC 2, we find a delayed echo in ISI 21 output. Similarly, an echo is discernible in ISI 31 at the same time. However, these measurements are not used for locking; consequently, the pulse does not propagate further. Figure 22 shows the TDI X time series for this pulse test in blue. The total TTL contribution, X^{TTL}, computed using the true coefficient values, is shown as the dashed red line. Their difference is shown in black, denoted as $X^{\mathrm{true}}_{\mathrm{corr}}$. We conclude that the subtraction is also effective in the presence of such MOSA pulses.

To understand the occurrence of the pulse and its echos in the TTL in TDI time series of Fig. 22 for example, let us evaluate Eq. (7) for the case of the example pulse occurring on MOSA 31 along φ while neglecting the other jitters. We then have to consider only the following TTL contributions:

$$\begin{aligned}\hat{x}_{\mathrm{TTL}_{31}} &= C_{31\varphi\mathrm{Rx}} \cdot \varphi^{\mathrm{DWS}}_{31} \\ \hat{x}_{\mathrm{TTL}_{13}} &= C_{31\varphi\mathrm{Tx}} \cdot \mathcal{D}_{13}\varphi^{\mathrm{DWS}}_{31}. \end{aligned} \tag{C1}$$

These two terms then contribute to the intermediate TDI variables $\bar{\eta}_{13}$ and $\bar{\eta}_{31}$. From Eqs. (10) and (14), we find that:

$$\begin{aligned} X^{\mathrm{TTL}} &= \mathrm{TDI}X(\hat{x}_{\mathrm{TTL}_{31}}, \hat{x}_{\mathrm{TTL}_{13}}) \\ &= (1 - \mathcal{D}_{12}\mathcal{D}_{21} - \mathcal{D}_{12}\mathcal{D}_{21}\mathcal{D}_{13}\mathcal{D}_{31} \\ &\quad + \mathcal{D}_{13}\mathcal{D}_{31}\mathcal{D}_{12}\mathcal{D}_{21}\mathcal{D}_{12}\mathcal{D}_{21}) \cdot (\hat{x}_{\mathrm{TTL}_{13}} + \mathcal{D}_{13}\hat{x}_{\mathrm{TTL}_{31}}) \\ &\propto (1 - \mathcal{D}_{12}\mathcal{D}_{21} - \mathcal{D}_{12}\mathcal{D}_{21}\mathcal{D}_{13}\mathcal{D}_{31} \\ &\quad + \mathcal{D}_{13}\mathcal{D}_{31}\mathcal{D}_{12}\mathcal{D}_{21}\mathcal{D}_{12}\mathcal{D}_{21}) \cdot \mathcal{D}_{13}\varphi^{\mathrm{DWS}}_{31}. \end{aligned} \tag{C2}$$

Therefore, the propagation of TTL through TDI results into the original pulse in MOSA 31 delayed by the light travel time along the arm 13, followed by three echos which occur at the time according to the multiple delays applied as in Eq. (C2). An effect of the locking is that the pulse is also discernible in ISI 12 and 21 (see Fig. 21) and thus also contributes to $\bar{\eta}_{12}$ and $\bar{\eta}_{21}$. However, these echos cancel as part of the TDI algorithm and thus do not have to be considered to explain the TTL after the application of TDI as shown in Fig. 22. In this example test, TDI Y and Z differ from TDI X. More specifically, while MOSA 31 does not contribute to the TTL in TDI Y, TDI Z contains 5 pulses. In general, the number of pulses discernible in each of TDI X, Y and Z depends on which of the six MOSA is jittering. Moreover, this visualization might look different if the laser locking efficiency were simulated more realistically, similarly if the simulated DWS measurements were affected by the locking. However, this is beyond the scope of this publication.

[1] P. Amaro-Seoane *et al.*, Laser interferometer space antenna, arXiv:1702.00786.

[2] M. Tinto and S. V. Dhurandhar, Time-delay interferometry, Living Rev. Relativity **24**, 1 (2021).

[3] S. Babak, M. Hewitson, and A. Petiteau, LISA sensitivity and SNR calculations, arXiv:2108.01167.

[4] G. Wanner and N. Karnesis on behalf of the LISA Pathfinder Collaboration, Preliminary results on the suppression of sensing cross-talk in LISA Pathfinder, J. Phys. Conf. Ser. **840**, 012043 (2017).

[5] M.-S. Hartig, S. Schuster, and G. Wanner, Geometric tilt-to-length coupling in precision interferometry: Mechanisms and analytical descriptions, J. Opt. **24**, 065601 (2022).

[6] Cross-talk in LISA: Tilt-to-length coupling in the TDI observables (to be published).

[7] E. Morrison, B. J. Meers, D. I. Robertson, and H. Ward, Automatic alignment of optical interferometers, Appl. Opt. **33**, 5041 (1994).

[8] J.-B. Bayle, O. Hartwig, and M. Staab, Adapting time-delay interferometry for LISA data in frequency, Phys. Rev. D **104**, 023006 (2021).

[9] J.-B. Bayle, Simulation and data analysis for LISA, Ph.D. thesis, Université de Paris, 2019, https://hal.archives-ouvertes.fr/tel-03120731/document.

[10] N. Houba, S. Delchambre, T. Ziegler, and W. Fichter, Optimal estimation of tilt-to-length noise for spaceborne

gravitational-wave observatories, J. Guid. Control Dyn. **45**, 1078 (2022).
[11] J. Bayle, A. Hees, and M. Lilley, LISA orbits (2021), gitlab.in2p3.fr/lisa-simulation/orbits.
[12] T. A. Prince, M. Tinto, S. L. Larson, and J. W. Armstrong, LISA optimal sensitivity, Phys. Rev. D **66**, 122002 (2002).
[13] M. Nofrarias, C. Röver, M. Hewitson, A. Monsky, G. Heinzel, K. Danzmann, L. Ferraioli, M. Hueller, and S. Vitale, Bayesian parameter estimation in the second LISA Pathfinder mock data challenge, Phys. Rev. D **82**, 122002 (2010).
[14] M. Armano *et al.*, Calibrating the system dynamics of LISA Pathfinder, Phys. Rev. D **97**, 122002 (2018).
[15] P. L. Bender, Wavefront distortion and beam pointing for LISA, Classical Quantum Gravity **22**, S339 (2005).
[16] C. P. Sasso, G. Mana, and S. Mottini, Coupling of wavefront errors and jitter in the LISA interferometer: Far-field propagation, Classical Quantum Gravity **35**, 185013 (2018).
[17] Y. Wang, G. Heinzel, and K. Danzmann, First stage of LISA data processing: Clock synchronization and arm-length determination via a hybrid-extended Kalman filter, Phys. Rev. D **90**, 064016 (2014).
[18] M. Hewitson *et al.*, Data analysis for the LISA Technology Package, Classical Quantum Gravity **26**, 094003 (2009).
[19] S. Barke, Inter-spacecraft frequency distribution for future gravitational wave observatories, Ph.D. thesis, Leibniz Universität Hannover, 2015.
[20] S. R. Hinton, ChainConsumer, J. Open Source Software **1**, 45 (2016).
[21] M. Tinto, F. B. Estabrook, and J. W. Armstrong, Time delay interferometry with moving spacecraft arrays, Phys. Rev. D **69**, 082001 (2004).
[22] O. Hartwig and M. Muratore, Characterization of time delay interferometry combinations for the LISA instrument noise, Phys. Rev. D **105**, 062006 (2022).
[23] H. Audley *et al.*, LISA Pathfinder mission extension report for the German contribution, Technical Report No. 50OQ1601, Max-Planck-Institut für Gravitationsphysik, Hannover, 2020, 10.2314/KXP:1692401564.
[24] M.-S. Hartig, Tilt-To-Length coupling in LISA Pathfinder: Model, data analysis and take-away messages for LISA, Ph.D. thesis, Leibniz Universität Hannover, 2022, 10.15488/12113.
[25] H. Wegener, V. Müller, G. Heinzel, and M. Misfeldt, Tilt-to-length coupling in the GRACE follow-on laser ranging interferometer, J. Spacecr. Rockets **57**, 1362 (2020).
[26] N. Messied, Deriving manoeuvre amplitude and frequency in LISA spacecraft from its geometry and thrusters, Master's thesis, 2021.
[27] J. N. Franklin, Numerical Simulation of stationary and non-stationary gaussian random processes, SIAM Rev. **7**, 68 (1965).